Dynamics of a single red blood cell in simple shear flow

Kushal Sinha and Michael D. Graham*

Department of Chemical and Biological Engineering, University of Wisconsin—Madison, Madison, Wisconsin 53706-1691, USA

(Received 23 December 2014; revised manuscript received 1 September 2015; published 20 October 2015)

This work describes simulations of a red blood cell (RBC) in simple shear flow, focusing on the dependence of the cell dynamics on the spontaneous curvature of the membrane. The results show that an oblate spheroidal spontaneous curvature maintains the dimple of the RBC during tank-treading dynamics as well as exhibits off-shear-plane tumbling consistent with the experimental observations of Dupire *et al.* [J. Dupire, M. Socol, and A. Viallat, Proc. Natl. Acad. Sci. USA **109**, 20808 (2012)] and their hypothesis of an inhomogeneous spontaneous shape. As the flow strength (capillary number Ca) is increased at a particular viscosity ratio between inner and outer fluid, the dynamics undergo transitions in the following sequence: tumbling, kayaking or rolling, tilted tank-treading, oscillating-swinging, swinging, and tank-treading. The tilted tank-treading (or spinning frisbee) regime has been previously observed in experiments but not in simulations. Two distinct classes of regime are identified: a membrane reorientation regime, where the part of membrane that is at the dimple at rest moves to the rim and vice versa, is observed in motions at high Ca such as tilted tank-treading, oscillating-swinging, swinging, and tank-treading, and a nonreorientation regime, where the part of the membrane starting from the dimple stays at the dimple, is observed in motions at low Ca such as rolling, tumbling, kayaking, and flip-flopping.

DOI: 10.1103/PhysRevE.92.042710 PACS number(s): 83.80.Lz, 83.10.Bb, 83.10.Pp, 47.11.Hj

I. INTRODUCTION

Experiments in the past several decades have established that in shear flow at low shear rates a suspended red blood cell (RBC) behaves as a rigid body and undergoes a tumbling motion (here denoted TU) [1], while at higher shear rates in a sufficiently viscous fluid its orientation takes on a constant angle with respect to the flow direction and the membrane rotates about the interior in a so-called tank-treading (TT) motion [1–4]. More detailed observations have revealed a number of variations on these basic motions. Goldsmith and Marlow [1] observed a rolling motion of the RBC in which the axis of revolution of the RBC is oriented in the vorticity direction of shear flow. Bitbol [5] and Yao *et al.* [6] made very similar observations. Recently, Abkarian *et al.* [7] reported a swinging motion in which the orientation of the cell oscillates about a fixed angle while simultaneously tank-treading. It has been shown by Dupire *et al.* [8,9] that there are domains in the parameter space in which the RBC dynamics is chaotic and dependent on the initial conditions. They also showed that during motions such as tumbling the cell is not necessarily reflection symmetric with respect to the shear plane. The observation of this wide array of motions even for an isolated particle in a simple flow field raises serious challenges for computational and theoretical approaches to the understanding of RBC dynamics in flow. The aim of this work is to understand the dependence of dynamical motion on the specifics of the membrane as well as the flow properties.

Jeffery analyzed the motion of a rigid axisymmetric particle in simple shear in the absence of fluid or particle inertia [10]. The particle will take on one of infinitely many periodic orbits, depending on its initial orientation. Each orbit is characterized by an orbit constant C that can take values in $0 \leqslant C < \infty$; when $C = 0$ the axis of revolution aligns with the vorticity direction for all time and the particle rolls, and when $C = \infty$ the axis of revolution traces out the unit circle on the shear plane and the particle tumbles. For intermediate values of C, the particle undergoes what is often called a kayaking motion during which the axis of revolution of the particle rotates about the vorticity axis. Some motions of RBCs are similar to Jeffery orbits, but many, such as tank-treading or swinging are not—further examples of motions that cannot be mapped onto Jeffery orbits are described below. An important first step in understanding the dynamics of fluid-filled deformable particles such as capsules, vesicles, and cells was taken by Keller and Skalak [11] (KS), who studied a model of a fluid-filled ellipsoid in shear. For an ellipsoid of a given shape, by equating the rate of work done by the external fluid with the rate of energy dissipation in the internal fluid, they were able to predict a transition between a tumbling motion (as would happen for a rigid ellipsoid) to a tank-treading motion, as the viscosity of the inner fluid was decreased. Skotheim and Secomb [12] and Abkarian *et al.* [7] extended the KS theory by introducing an elastic membrane to the ellipsoidal particle model and were able to predict an additional "swinging" motion, as well as intermittency during the transitions between different motions. It should be noted that the KS theory and its variants are two dimensional, so out-of-shear plane RBC motions such as those observed by Dupire *et al.* [9] cannot be predicted.

A number of efforts have been made to understand the complex RBC dynamics in shear flow via detailed direct simulations of the fluid and membrane dynamics. To model the RBC appropriately, five key features need to be specified: (i) the viscosity ratio λ between the inner and outer fluids, (ii) the biconcave rest shape of the cell, (iii) viscoelasticity [13,14] of the RBC membrane, (iv) the natural state of each point on the RBC membrane, and (v) constitutive equations for stretching (tangential) and bending (normal) elasticity. Research over the past several decades has settled the first two points; however, the last three are still under active study. The present work focuses on the last two points.

*Corresponding author: mdgraham@wisc.edu

To help clarify nomenclature we pause at this point to provide a number of definitions. In general a *natural shape* or *natural state* for an element of an elastic material is one from which any deformation would lead to elastic restoring forces. For a complex structure such as an RBC membrane it is possible that the natural shape for shear elasticity (tangential deformations) may differ from that for bending elasticity (normal deformations) so the overall natural shape of an element results from the balance of bending and shear forces. Consistent with usage in the vesicle literature as described below, we denote the natural shape for bending elasticity as the *spontaneous curvature*. Finally, the *equilibrium shape* or *rest shape* of the RBC is determined by the interplay between membrane area, enclosed volume, and membrane mechanics. At rest, elements of the membrane could be under stress (i.e., not in their natural state), but the forces acting on all elements are in equilibrium.

Early work of Goldsmith and Marlow [1] and recent experiments of Dupire *et al.* [9] showed that the RBC maintains its biconcave shape even during tank-treading and hypothesized that this effect may come from anisotropic elastic properties or an inhomogeneous natural shape. Similarly, it had been noted earlier by Fischer [15] that RBCs have "shape memory" after experimentally observing that the same part of the membrane forms the dimple after constant shearing for many hours. The return of material points to the same positions relative to the equilibrium shape of the cell implies that material elements at different positions have different natural shapes. Shape memory could arise from spatial variations in either the natural state for shear elasticity or for bending elasticity or both.

In a first attempt to explain the biconcave shape of the RBC, Canham [16] proposed that the minimization of bending energy of the membrane would explain the stability of the biconcave shape. However, starting from the same volume, oblate and prolate spheroids will evolve into a biconcave discoid and a dumbbell, respectively, as volume is reduced, with a dumbbell shape having lower energy and thus being a more stable shape; this is the opposite of what one is looking for. Helfrich *et al.* [17–19] suggested the need for a spontaneous curvature having a negative value such that a biconcave shape is stable. In these and many subsequent treatments, the spontaneous curvature was assumed to be constant over the entire surface and treated as a free parameter that can be chosen in order to fit the RBC shape. Zarda *et al.* [20] studied both biconcave and spherical spontaneous shapes and concluded that for a spherical shape, an unrealistically high value of bending modulus would be required to explain the experimentally observed shape of osmotically swollen RBCs. A biconcave spontaneous shape on the other hand is able to reproduce experimental swollen shapes in the range of experimentally observed bending modulus. Fischer *et al.* [21] concluded that neither proposal of sphere or biconcave spontaneous shape explains all the shapes obtained in the swelling experiment of the RBC but inclined toward the biconcave shape as it reproduces shapes observed in swelling experiment for the experimentally known shear and bending moduli.

Using an area-difference-elasticity (ADE) model that, in addition to including shear and bending elasticity also takes account of the change in area of the inner and outer leaflets of the cell membrane, Lim *et al.* [22] showed that the biconcave equilibrium shape is reached starting from an oblate spheroid having the same surface area A as the RBC and reduced volume $V_0[= V_{\mathrm{ob}}/(A^{3/2}/3\sqrt{4\pi})]$ of 0.95, where V_{ob} is the volume of oblate spheroid. If an oblate spheroid is indeed the spontaneous shape, then the resulting curvature would not be uniform over the surface. Note that a spontaneous shape that is spatially varying (like an oblate spheroid) but still close to a sphere leads to a low energy barrier between dimple and rim due to weak inhomogeneity, such that weak shear flow may generate tank treading during which the biconcave shape is preserved. The choice of spontaneous shape is still far from settled and future experiments may shed some light on the issue. In this work, we will address the issue of spatially varying spontaneous membrane curvature and how it will affect the dynamics of the RBC under simple shear flow.

Now we turn to a brief review of simulations of RBCs in shear. Although attempts to understand the RBC dynamics numerically spans the past two decades [23–30], most of these works focused primarily on RBC dynamics in the case where the RBC shape is symmetric across the shear plane (or the dimple is centered on the shear plane). Recently, Dupont *et al.* [31] showed that an elastic capsule with a prolate spheroid rest shape with its axis of symmetry oriented off of the shear plane will reach a unique final dynamical motion for all initial orientations. Depending on Ca, they reported three final dynamical states: (i) rolling for lower Ca, (ii) wobbling in which capsule precesses around vorticity axis as Ca is increased, and (iii) a swinging-oscillating motion in which the long axis of capsule oscillates around the shear plane with amplitude of oscillation decreasing with increase in Ca and resulting in a in-plane swinging motion at high Ca. Wang *et al.* [32] studied off-plane motion of oblate and prolate capsules and concluded that the final dynamical state could depend on the initial inclination angle. Similarly, Cordosco and Bagchi [33] reported off-plane motion of oblate, prolate, and biconcave capsules. Unlike Dupont *et al.* [31] and Wang *et al.* [32], they included membrane bending stiffness in their formulation and considered a spatially uniform spontaneous curvature in case of biconcave capsules. They observed rolling as a dominant mode in the physiological relevant viscosity ratio case $\lambda \sim 5$, tank-treading or wobbling mode at $\lambda < 1$ and an intermittent regime at low Ca and low λ where dynamics are dependent on initial orientation. It has to be noted that both Bitbol [5] and Dupire *et al.* [9] experimentally observed rolling dynamics in a dextran solution where the viscosity ratio was less than unity. The discrepancy between simulation and experiment may result from the use of a spatially uniform spontaneous curvature that corresponds to a biconcave shape [34]. In order to model the RBC membrane correctly, an assumption of the spontaneous shape has to be made and finding the appropriate shape has been a challenge for both theoreticians and experimentalists.

Recently, attempts were made to understand the effect of spontaneous shape on the final dynamics of the RBC. Peng *et al.* [35] studied the effect of the nonbiconcave spontaneous shape on the RBC dynamics and concluded that for a RBC to retain its biconcave shape during tank-treading, as pointed out by Dupire *et al.* [9], the spontaneous curvature has to be

nonbiconcave. With a biconcave spontaneous curvature, under no condition were they able to achieve tank-treading without significantly disturbing the initial shape. Cordosco *et al.* [36] also studied nonbiconcave spontaneous shapes and concluded that the spontaneous shape makes a significant difference in cell dynamics depending upon the viscosity ratio. They saw the dimple in the RBC remain intact for both the biconcave and oblate spontaneous shapes. Though Peng *et al.* and Cordasco *et al.* explored RBC dynamics with nonbiconcave spontaneous curvature, in both works, they imposed a spatially uniform spontaneous curvature c_0.

RBC membranes differ from model lipid bilayers in that they have embedded proteins with an underlying spectrin cytoskeleton and an asymmetric bilayer leaflet composition [37]; all of these have been shown to modify c_0 [38–41]. In particular, proteins have been shown to preferentially bind via curvature-sensing mechanism [42]. Based on this evidence, one may argue c_0 will be spatially inhomogeneous. Though shape memory originating from shear elastic energy is expected to be dominant, we show that the shape memory arising from the inhomogeneity in the spontaneous curvature plays an important role as well.

One possible reason for this counterintuitive result is that all the nontrivial dynamics of a deformable RBC in flow might be viewed in the following light: The dynamics of a *rigid* RBC in shear are highly degenerate, because there are infinitely many possible Jeffery orbits for the cell to follow, each corresponding to a different orbit constant. This degeneracy is a consequence of the Stokes flow reversibility constraint for a rigid object in flow, and deformability removes this constraint, breaking the degeneracy. *How* this degeneracy is broken depends on the specific details of the elasticity of the cell: evidently, different elastic behavior can break the degeneracy in different ways.

In the present work we focus on how RBC dynamics in shear depend on the specifics of the model, e.g., spontaneous curvature as well as parameters such as Ca, λ, and initial orientation. The rest of the paper is organized as follows: in Sec. II, we present the RBC model and the numerical algorithm. This is followed by the validation of our numerical method for bending calculation and RBC model in Sec. III. Next, in Sec. IV we present detailed results of single RBC dynamics in simple shear flow. Concluding remarks are presented in Sec. V.

II. MODEL FORMULATION

A. Red blood cell model

We consider an isolated fluid-filled deformable cell with a biconcave discoid rest shape between two parallel plates in linear shear flow as shown in Fig. 1. The plates are far enough apart that the simulations essentially represent the result for the unbounded domain. The discoid radius is a, which for a human RBC is about 3.9 μm; further discussion of how the rest shape of the cell is specified will be given below. The undisturbed flow velocity in simple shear flow is given as $u = \dot{\gamma} y$, where $\dot{\gamma}$ is the wall shear rate. The interior and suspending fluids are assumed to be incompressible and Newtonian with viscosity $\lambda\mu$ and μ, respectively. The suspending fluid, blood plasma, is generally considered to

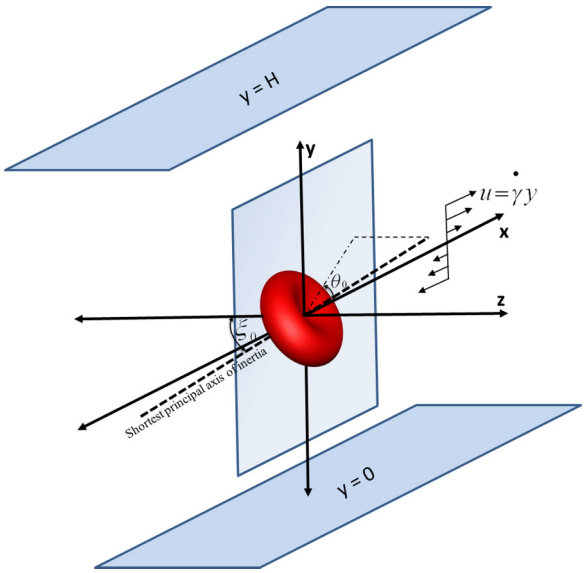

FIG. 1. (Color online) Schematic of the 3D orientation of an RBC. The initial angle between the shortest principal axis of inertia ψ_3 of the RBC and the vorticity direction (z axis) is ξ_0, and the angle between the flow direction (x axis) and the projection of the axis of revolution onto the shear plane is θ_0.

have viscosity of about 1.10–1.35 mPa s [43] and the interior cytoplasmic viscosity is 5.8–5.95 mPa s [44,45]. The RBC membrane is a lipid bilayer with embedded lipids and proteins and an underlying spectrin protein layer. It has a thickness of about 4 nm [46] and can be considered as a thin and soft shell. Its mechanical response can be split into in-plane shear elasticity and out-of-plane bending elasticity. The membrane in-plane shear elasticity modulus $G \sim 2.5$–6 μN/m [47,48] while its bending modulus $K_B \sim 2.7$–9×10^{-19} N m [49,50] ~65–215 k_BT, where k_B is the Boltzmann constant and T is the temperature. (Thus thermal fluctuations can usually be neglected at room temperature.) The shear modulus of the RBC will be expressed by the nondimensional capillary number $\mathrm{Ca} = \mu\dot{\gamma}a/G$. The bending modulus of the RBC is expressed nondimensionally by $\hat{\kappa}_B = K_B/a^2G$, which is $O(10^{-3}$–$10^{-2})$, so bending is often neglected in numerical models. Nevertheless, there are several physical mechanisms [51,52] for bending moments to develop over the RBC surface. A number of studies have shown bending to affect shape [53,54] and dynamics [55,56]; our goal is to systematically examine the effect of the bending stresses and spontaneous curvature on the RBC dynamics. Dynamical modes presented in Sec. IV A show dependence on bending modulus $\hat{\kappa}_B$ as well. Furthermore, incorporation of bending is important in simulations because it prevents numerical buckling and wrinkling of the membrane [57]. Hence, bending energy is included in our formulation. We take $\hat{\kappa}_B = 0.03$, which corresponds to $K_B \sim 11 \times 10^{-19}$ Nm.

The total strain energy of the RBC membrane Γ can be written as:

$$E = \frac{K_B}{2}\int_\Gamma (2\kappa_H + c_0)^2 dS + \overline{K_B}\int_\Gamma \kappa_G dS + \int_\Gamma W dS, \quad (1)$$

where κ_H, κ_G are the mean and Gaussian curvature of the surface, respectively; K_B and $\overline{K_B}$ are the bending moduli; c_0

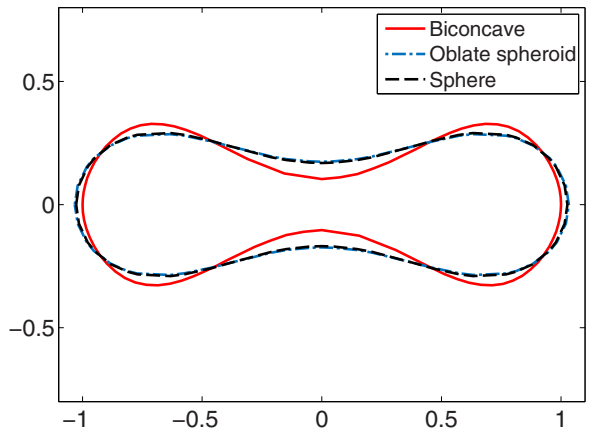

FIG. 2. (Color online) The final rest shape of an RBC when spontaneous shape is chosen to be either oblate spheroid or sphere compared to Evans *et al.* [60]. The rest shape when a biconcave discoid is the spontaneous shape is unchanged from its starting Evans *et al.* shape.

is the spontaneous curvature, defined as $c_0 = -2H_0$, where H_0 is the mean curvature of the spontaneous shape; and W is the shear strain energy density. In Eq. (1), the first two terms come from the bending or Canham-Helfrich energy [16,17] and the third term represents the shear strain energy stored in the RBC membrane. Several models for W are studied, as we discuss below. There is a strong energy penalty for local area change in these models but a strict inextensibility constraint is not imposed.

The first variation of total energy E gives the total membrane strain force density $\boldsymbol{f}^m$,

$$\boldsymbol{f}^m = \boldsymbol{f}^b + \boldsymbol{f}^s, \tag{2}$$

where $\boldsymbol{f}^b$ and $\boldsymbol{f}^s$ are bending and shear elastic force densities, respectively. These are further discussed below and in the Appendix. Note that the bending energy leads to forces both normal and tangential to the membrane while the in-plane strain energy leads only to a tangential force.

It should be noted that the equilibrium rest shape of the membrane can differ from the spontaneous shape. In the case where the natural shape for shear elasticity and the spontaneous shape for bending elasticity are not the same, the membrane is under stress even at rest. Indeed, micropipette and fluorescence imaging experiments [58] and subsequent Monte Carlo simulations [59] suggest the presence of residual stress in the rest state. For our model, Fig. 2 shows the equilibrium shape with an initial biconcave shape and three different spontaneous shapes for the bending elasticity: (i) sphere, (ii) oblate spheroid, and (iii) biconcave discoid. In the biconcave discoid case, the expression of Evans and Fung [60] is used:

$$y = \frac{a}{2}\sqrt{1-r^2}(C_0 + C_2 r^2 + C_4 r^4), \tag{3}$$

where $r^2 = x^2 + z^2 \leqslant 1$, $C_0 = 0.2072$, $C_1 = 2.0026$, and $C_2 = -1.1228$. The biconcave discoid shape is used as natural shape for shear elasticity in all the cases. The reduced volume V_0 for the oblate spheroid [case (ii)] is 0.95. The major axis a of oblate spheroid is kept same as nominal radius of the biconcave shape. As seen in Fig. 2, even when the spontaneous shape is a sphere or oblate spheroid, the equilibrium rest shape is still a biconcave discoid; the net effect of a nonbiconcave spontaneous shape is a slightly more shallow dimple.

We now address the evaluation of bending force density, $\boldsymbol{f}^b$. The Gauss-Bonnet theorem ensures that the second term in Eq. (1) is a constant when no topological changes are involved. Thus, there is no force density associated with that term. The force density due to bending is thus given by first variation of first term in Eq. (1). We have built on the previous work of Zhong *et al.* [61] and Capovilla *et al.* [62] and extended their result to include a spatially varying c_0. The revised Zhong-Helfrich expression in our formulation for the force density is given as:

$$\boldsymbol{f}^b = K_B\big\{\big[\Delta_s(2\kappa_H + c_0) + (2\kappa_H + c_0)\big(2\kappa_H^2 - 2\kappa_G - c_0\kappa_H\big)\big]\boldsymbol{n} + \tfrac{1}{2}\nabla_s(2\kappa_H + c_0)^2\big\}, \tag{4}$$

where Δ_s is the Laplace-Beltrami operator, $\boldsymbol{n}$ is the outward normal to the surface, and ∇_s is the surface gradient operator (see the Appendix for derivation). The last term gives the tangential force density coming from the Canham-Helfrich Hamiltonian. An equivalent expression of force density for the case of inhomogeneous c_0 can be seen in the work of Zhao [26] *et al.* where they chose biconcave discoid as the spontaneous shape. Note that the bending energy leads to forces both normal and tangential to the membrane while the in-plane strain energy leads only to a tangential force.

This tangential term is absent in most studies of vesicle and cell motion. In the case of perfectly incompressible membranes, it can be absorbed into the Lagrange multiplier that enforces the constant-area constraint (just as in the rotation form of the incompressible Navier-Stokes equations the kinetic energy density can be absorbed into the pressure [63]). In the present formulation, where this constraint is not strictly enforced, we find that nevertheless the tangential force arising from the in-plane strain energy (described below) is completely dominant over this term—whether we include it or not makes no discernible difference to the dynamics.

In contrast, the normal force associated with the bending energy has a non-negligible effect on the dynamics; recall that the force resulting from the in-plane strain energy has no normal component so even a small bending energy might be expected to have noticeable effects. Specifically, as noted above, if bending energy is neglected entirely, then membranes will sometimes wrinkle at the scale of the mesh. Further, we briefly illustrate in Sec. IV A that changes in K_B can qualitatively affect the dynamics.

Next, we describe the calculation of the in-plane shear elastic force density, $\boldsymbol{f}^s$. We note that the strain-energy density W of the membrane is a function of the principal stretch ratios, λ_1 and λ_2. Three commonly used membrane models will be studied: (i) the Skalak model, originally proposed for the RBC membrane by Skalak *et al.* [64], which is strain hardening and can be parametrized to yield a strong resistance to area change relative to its resistance for shear deformation, consistent with the area incompressibility of a lipid bilayer; (ii) the neo-Hookean model, which mimics the behavior of the cross-linked rubberlike materials and is strain softening, and (iii) the Yeoh model, which was originally proposed for the

vulcanized rubber and recently used for comparison with RBC optical tweezer experimental data of Mills *et al.* [48,65]

The Skalak model [64] has the strain energy density given by

$$W_{\mathrm{SK}} = \frac{G}{4}\left[\left(I_1^2 + 2I_1 - 2I_2\right) + CI_2^2\right]. \tag{5}$$

The two invariants, I_1 and I_2, are given by

$$I_1 = \lambda_1^2 + \lambda_2^2 - 2, \quad I_2 = \lambda_1^2\lambda_2^2 - 1. \tag{6}$$

The parameter C characterizes the energy penalty for area change. It has been shown that under a simple uniaxial deformation, the results for the Skalak model reach an asymptotic value [66] for $C \geqslant 10$. Following Barthes-Biesel *et al.* [66], for a neo-Hookean model the strain energy density function is given by

$$W_{\mathrm{NH}} = \frac{G}{2}\left(I_1 - 1 + \frac{1}{I_2 + 1}\right). \tag{7}$$

For the Yeoh model, which can be viewed as a cubic extension of the neo-Hookean model, the membrane strain energy density is given as [48,67]

$$W_{\mathrm{YE}} = \frac{G}{2}\left(I_1 - 1 + \frac{1}{I_2 + 1}\right) + \frac{G}{30}\left(I_1 - 1 + \frac{1}{I_2 + 1}\right)^3. \tag{8}$$

The Yeoh model behaves like the neo-Hookean model at small deformations but, due to the higher-order term, its strain-hardening or strain-softening behavior varies with deformation depending on the coefficients of the higher-order term. We use the Mills *et al.* [48] formulation, which is strain softening at moderate deformations and strain hardening at large deformations. The resultant force $\boldsymbol{f}^s$ is calculated using the principle of virtual work. We do this in the context of the discretized surface as described in the following subsection.

B. Discretization

The surface is discretized into piecewise flat triangular elements. As seen in Eq. (4), in order to calculate the bending force, we require the knowledge of the curvatures and normal of the surface, which must be approximated here based on the piecewise flat discretization. To do so, we use an approach given by Meyer *et al.* [68] which defines these properties of a continuous surface as spatial averages. The averaging is done within the immediately neighboring triangles, denoted the one-ring neighborhood (see Fig. 3). We select a local surface patch, $\mathcal{A}_M$, in the one-ring neighborhood whose contour passes through the circumcenter (meeting point of perpendicular bisectors of the sides of a triangle) of acute triangles or through the midpoint of the side opposite to an obtuse angle of obtuse triangles—see Fig. 3. Choosing the surface patch $\mathcal{A}_M$ in this way minimizes the error associated with the spatial averaging. The area of this patch is denoted A_{Mixed}. An algorithm to calculate A_{Mixed} is given by Meyer *et al.* [68].

The surface Laplacian of position along the surface is: $\Delta_s \mathbf{x} = 2\kappa_H \mathbf{n} = \mathbf{K}(\mathbf{x})$, where κ_H is the local mean curvature, $\mathbf{n}$ is the normal to the surface, and $\mathbf{K}$ is the discretized curvature

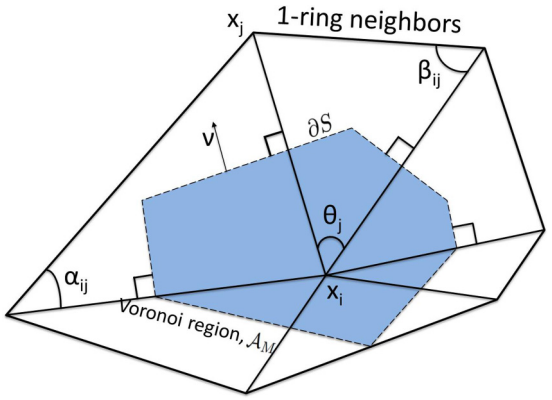

FIG. 3. (Color online) Schematic of the one-ring neighborhood of node $\mathbf{x}_i$ used to calculate $\mathbf{f}_i^b$ in Eq. (16). Here the solid boundary represents the one-ring neighborhood of node $\mathbf{x}_i$ while the shaded region represents the mixed Voronoi patch $\mathcal{A}_{Mi}$ with contour ∂S_i represented by dashed curve. The area of shaded region is $\mathcal{A}_{\mathrm{Mixed}}$. Note that for creating $\mathcal{A}_{Mi}$, the circumcenter is chosen if it is an acute-angled triangle and midpoint of the side opposite the obtuse angle in an obtuse-angled triangle. α_{ij}, β_{ij} are angles opposite to the common shared edge $(\mathbf{x}_i, \mathbf{x}_j)$ and θ_j is the angle subtended at node i by face j. The normal to the contour ∂S_i is $\boldsymbol{\nu}$.

vector. It has been shown [68] that $\mathbf{K}(x_i)$ is given by:

$$\mathbf{K}(x_i) = \frac{1}{2A_{\mathrm{Mixed}}} \sum_{j \in N_1(i)} (\cot\alpha_{ij} + \cot\beta_{ij})(\mathbf{x}_i - \mathbf{x}_j), \tag{9}$$

where α_{ij} and β_{ij} are the two angles opposite to the edge in the two triangles sharing the edge $(\mathbf{x}_i, \mathbf{x}_j)$ and $N_1(i)$ is the set of one-ring neighbor vertices of the vertex i. The normal vector and mean curvature at a node on membrane surface are given, respectively, by:

$$\begin{aligned} \mathbf{n}(x_i) &= \frac{\mathbf{K}(x_i)}{\|\mathbf{K}(x_i)\|}, \\ \langle \kappa_{Hi}(x_i) \rangle &= \frac{1}{2}\|\mathbf{K}(x_i)\|. \end{aligned} \tag{10}$$

Here $\langle \cdot \rangle$ represents an area averaged quantity. To calculate $\Delta_s \kappa_H$, we interpolate the nodal values of κ_{Hi} over the triangular element E. If ξ and η are the natural coordinates of the element E, then its mean curvature can be written as:

$$\kappa_H{}^E(\xi, \eta) = \sum_{n \in E} \phi_i^E(\xi, \eta)\kappa_{Hi}, \tag{11}$$

where ϕ_i^E are basis functions associated with the nodes of triangle and are given by $\phi_1^E = \xi, \phi_2^E = \eta$ and $\phi_3^E = 1 - \xi - \eta$. The surface gradient of mean curvature in E is

$$\nabla_s \kappa_H{}^E = \frac{\partial \kappa_H{}^E}{\partial \xi}\mathbf{g}^\xi + \frac{\partial \kappa_H{}^E}{\partial \eta}\mathbf{g}^\eta, \tag{12}$$

where $\mathbf{g}^\xi$ and $\mathbf{g}^\eta$ are the contravariant vectors for change of basis. Following Boedec *et al.* [69], we also use surface divergence theorem to get the mean value of the surface

Laplacian for the mean curvature as:

$$\begin{aligned}\Delta_s \kappa_H &= \frac{1}{A_{\text{Mixed}}}\int_{\mathcal{A}_{Mi}} \Delta_s \kappa_H dS \\ &= \frac{1}{A_{\text{Mixed}}}\int_{\mathcal{A}_{Mi}} \nabla_s \cdot (\nabla_s \kappa_H) dS \\ &= \frac{1}{A_{\text{Mixed}}}\int_{\partial S_i} \nabla_s \kappa_H \cdot \boldsymbol{\nu} dl. \end{aligned} \tag{13}$$

Here the last expression is the contour integral over $\mathcal{A}_{Mi}$ and $\boldsymbol{\nu}$ is the tangent vector to the surface, normal to the contour ∂S_i of $\mathcal{A}_{Mi}$ (see Fig. 3). The discrete version of Eq. (13) is given as:

$$\langle \Delta_s \kappa_H \rangle = \frac{1}{A_{\text{Mixed}}}\sum_{j=1}^{f_v} \nabla_s \kappa_H{}^{Ej} \cdot \boldsymbol{\nu}^{Ej} l_j, \tag{14}$$

where l_j is the length of the j-th face of $\mathcal{A}_{Mi}$ and f_v is the total number of faces in Voronoi region $\mathcal{A}_{Mi}$. We now need the Gaussian curvature, κ_G, to be able to calculate the bending force. A discrete version of Gauss-Bonnet theorem gives the Gaussian curvature [68]:

$$\langle \kappa_{Gi}(x_i) \rangle = \frac{1}{A_{\text{Mixed}}}\left(2\pi - \sum_{j=1}^{f_v} \theta_j\right), \tag{15}$$

where θ_j is the angle of the j-th face at vertex x_i in the one-ring neighborhood. It is noteworthy that Eq. (15) will return zero for any flat surface or a roof-shaped one-ring neighborhood. The discrete form of the bending force density at any node x_i on the surface is then given as:

$$\begin{aligned}\boldsymbol{f}_i^b = K_B[&\langle \Delta_s(2\kappa_H + c_0)\rangle + (2\langle \kappa_H\rangle + \langle c_0\rangle)(2\langle \kappa_H\rangle^2 \\ &- 2\langle \kappa_G\rangle - \langle c_0\rangle\langle \kappa_H\rangle)]\mathbf{n}. \end{aligned} \tag{16}$$

Next, we discuss our approach to compute in-plane shear force density. To describe the membrane surface of the RBCs, we adopt the finite-element method developed by Charrier *et al.* [70]. In the Charrier *et al.* [70] approach, the membrane forces are determined using the positions of the nodes in the deformed state relative to their positions in the natural state for shear elasticity by the application of the principal of virtual work, such that the computed forces and the known displacements are consistent with the strain energy stored in the element. The deformation at any point inside the element is calculated by interpolating linearly from the nodes. An arbitrarily oriented deformed element and the corresponding undeformed element are transformed to the same plane by rigid body rotations, using a transformation matrix $\mathbf{R}^E$ for each element E. Note that the rigid body rotations and translations have no effect on the strain energy and, consequently, the forces. The principal stretch ratios then can be calculated from the nodal displacements in the transformed plane. The local elastic forces at node i are given [70] as:

$$\boldsymbol{f}_i^L = \left(\frac{\partial W}{\partial \lambda_1}\frac{\partial \lambda_1}{\partial \boldsymbol{\epsilon}} + \frac{\partial W}{\partial \lambda_2}\frac{\partial \lambda_2}{\partial \boldsymbol{\epsilon}}\right), \tag{17}$$

Here $\boldsymbol{f}_i^L$ is the nodal force on the RBC surface and $\boldsymbol{\epsilon}$ is the displacement from the undeformed state. The global components of the nodal forces, $\boldsymbol{f}_i^E$, for an element are calculated by transforming them back. The total shear elastic force on a cell node is calculated as the sum of forces resulting from the deformations of triangular elements surrounding that node and is given by: $\boldsymbol{f}_i^s = \sum \boldsymbol{f}_i^E$, where the summation is over all triangular elements to which the node belongs.

The resultant membrane force density is the combination of out-of-plane bending and in-plane tension as given in Eq. (2). Here we assume that the entire shear elastic and bending energy stored in cell membrane has been reassigned to the vertices of the discretized triangular elements. In our boundary integral formulation for solving fluid velocity, we need the hydrodynamic traction jump $\Delta \boldsymbol{f}$ across the interface. As we neglect inertia and Brownian fluctuations of the membrane, the membrane equilibrium condition states that the total membrane force has to be balanced by the hydrodynamic traction jump across the interface, which gives $\Delta \boldsymbol{f}_i = -\boldsymbol{f}_i^m$.

C. Fluid velocity calculation

The radius a of the RBC is $\sim$3.9 μm, its velocity in the microcirculation $U \sim 100$–$1000\ \mu$m/s, the viscosity of plasma $\mu \sim 1.38$ mPa s, and its density $\rho \sim 10^3$ kg/m^3. These parameters yield a Reynolds number of the order 10^{-3}–10^{-2}, which we assume is sufficiently small that the fluid motion is governed by the Stokes equation. Under these assumptions, we can write the fluid velocity $\mathbf{u}$ at any point $\mathbf{x_0}$ in the problem domain in boundary integral form [71,72] as

$$u_j(\mathbf{x_0}) = u_j^{\infty}(\mathbf{x_0}) + \sum_{n=1}^{N_p}\int_{S^n} q_i(\mathbf{x}) G_{ji}(\mathbf{x_0},\mathbf{x}) dS(\mathbf{x}), \tag{18}$$

where $\boldsymbol{q}(\boldsymbol{x}_0)$ is a single layer density that satisfies (for $\boldsymbol{x}_0 \in S^n$)

$$\begin{aligned} q_j(\boldsymbol{x}_0) + \frac{\lambda-1}{4\pi(\lambda+1)} n_k(\boldsymbol{x}_0)\sum_{n=1}^{N_p}\int_{S^n} q_i(\mathbf{x}) T_{jik}(\mathbf{x_0},\mathbf{x}) dS(\mathbf{x}) \\ = -\frac{1}{4\pi\mu}\left[\frac{\Delta f_j(\boldsymbol{x}_0)}{\lambda+1} + \frac{\lambda-1}{\lambda+1} f_j{}^{\infty}(\boldsymbol{x}_0)\right]. \end{aligned} \tag{19}$$

Here $u^{\infty}(\mathbf{x_0})$ is the undisturbed fluid velocity at given point $\mathbf{x_0}$ while $f^{\infty}(\mathbf{x_0})$ is the traction at a given point (computed with the suspending fluid viscosity μ) due to the stress generated in the fluid corresponding to the undisturbed flow $u^{\infty}(\mathbf{x_0})$, S^n denotes the surface of the particle n and $\Delta f(\mathbf{x})$ is the hydrodynamic traction jump across the interface. The Green's function and its associated stress tensor for the Stokes equation in the geometry of interest are $\mathbf{G}$ and $\mathbf{T}$, respectively. The Green's function $\mathbf{G}$ and associated stress tensor $\mathbf{T}$ are taken to satisfy the boundary conditions imposed at the system boundaries so the integrals involved in this formulation are over the internal (interfacial) boundaries only. The element nodes are taken to move with the local fluid velocity as required by the no-slip boundary condition. In the slit geometry, we have periodic boundary conditions in flow and vorticity direction, i.e., the x and z directions and the walls are in the y direction. We employ the no-slip boundary condition at two walls at $y = 0$ and $y = H$.

This boundary integral formulation slightly differs from the most commonly used approaches [71] but provides an advantage in that the multiplicand $\boldsymbol{q}(\boldsymbol{x})$ of both $\boldsymbol{G}(\boldsymbol{x}_0,x)$ and $\boldsymbol{T}(\boldsymbol{x}_0,x)$ is a function of the location of the source point $\boldsymbol{x}$ and thus allows us to use an accelerated method [72] tailored for

nonperiodic geeometries [72]. This approach is based on the general geometry Ewald-like method (GGEM) developed by Hernandez-Ortiz *et al.* [73], in which the key idea is to split a Dirac $delta$ force density $\delta(\mathbf{r})$ into a smooth quasi-Gaussian global density $\rho_g(\mathbf{r})$ and a second local density $\rho_l(\mathbf{r})$ given by following expressions:

$$\delta(\mathbf{r}) = \rho_l(\mathbf{r}) + \rho_g(\mathbf{r}), \tag{20a}$$

$$\rho_g(\mathbf{r}) = \frac{\alpha^3}{\pi^{3/2}} e^{-\alpha^2 r^2}\left(\frac{5}{2} - \alpha^2 r^2\right), \tag{20b}$$

$$\rho_l(\mathbf{r}) = \delta(\mathbf{r}) - \rho_g(\mathbf{r}), \tag{20c}$$

where α^{-1} is the length scale over which the global density varies and $\mathbf{r}$ is the position vector relative to the pole of the singularity. The solution associated with the local density is short ranged and can be neglected beyond a length scale of $O(\alpha^{-1})$ from its pole. It is obtained assuming free-space boundary conditions while the solution associated with global density is computed numerically ensuring that the boundary condition associated with the overall problem is satisfied [72,73]. In our implementation the periodic x and z directions are represented using a Fourier series while a Chebyshev spectral scheme is used for the y direction. Based on extensive tests in Ref. [72], we set $\alpha h_m = 0.5$ to minimize numerical error. Here h_m is mean mesh spacing associated with the global solution and α is taken as $4/a$. Kumar *et al.* [72] have shown that the computational cost associated with this method is $O(N \log N)$ for the slit geometry, where N is proportional to the product of total number of particles in system, N_p, and the number of triangular elements N_Δ on the particle surface.

Our simulation domain is a cubic box of size $12.5a$. We verified that the RBC dynamics remain unchanged in larger domains. Flow and vorticity directions are periodic and walls are present in the flow gradient direction at $y = 0$ and $y = H = 12.5a$. The RBC is placed at the center of box in all simulations. The surface of the RBC is discretized into $N_\Delta = 1280$ triangular elements. The surface element nodes are advanced in time using a second-order Adams-Bashforth method with time step $\Delta t = 0.01\mathrm{Ca}h$, where h is the minimum node-to-node distance. Time is nondimensionalized by the wall shear rate, $\dot{\gamma}$, and length is nondimensionalized by nominal radius of the RBC, a. All simulations reported here were performed on a single processor.

III. VALIDATION OF METHODS AND MODELS

A. Bending resistance validation

The accelerated boundary integral method with GGEM as well as the in-plane shear elasticity formulation have been extensively tested in prior work [72]. We validate our numerical algorithm for the effect of bending stiffness on the deformation of spherical capsules in the shear flow by comparison of results for spherical capsules for various $\hat{\kappa}_B$ with those of Le *et al.* [74]. In Fig. 4, we show steady-state values of Taylor deformation parameter D as a function of dimensionless shear rate Ca for $\lambda = 1$ and $\hat{\kappa}_B = 0$, 0.03, and 0.12; the closed symbols are the numerical results from Le *et al.* with an immersed boundary method and a Catmull-Clark subdivision scheme for surface discretization and the lines are from our simulations. Good agreement is found.

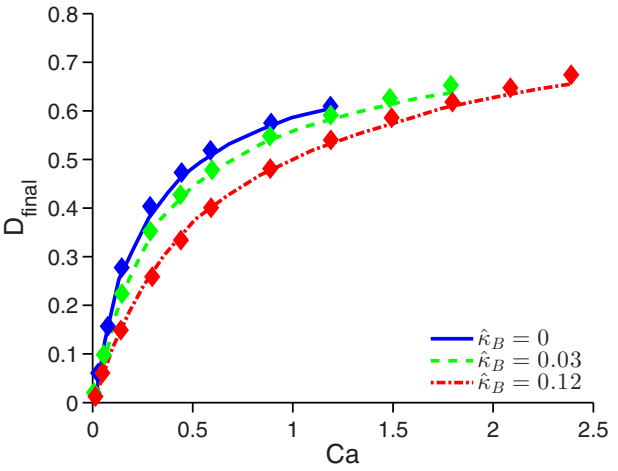

FIG. 4. (Color online) Steady-state Taylor deformation parameter for a spherical capsule with $\hat{\kappa}_B = 0,0.03,0.12$ as function of Ca, with $\lambda = 1$. Symbols are from Le *et al.* [74] and solid lines are our numerical results.

B. Red blood cell model validation

In recent work, Dimitrakopoulos [75] showed that large differences of shear modulus reported in various studies can be explained based on the different membrane laws and deformation regimes used to fit the experimental data. He analyzed four commonly used membrane laws: Skalak (SK), neo-Hookean (NH), Evans (EV), and Yeoh (YE). If one imposes the local area-incompressibility constraint $\lambda_1\lambda_2 = 1$ and matches the local tension for each law at same stretch ratio, then the shear modulus G of the RBC membrane calculated using these different membrane laws at moderate deformations (~40% extension) are related to the modulus for the Skalak model, G^{SK}, as follows:

$$G^{\mathrm{NH}} \approx 2G^{\mathrm{SK}}, \quad G^{\mathrm{YE}} \approx 1.90G^{\mathrm{SK}}, \quad \text{and } G^{\mathrm{EV}} \approx 2.67G^{\mathrm{SK}}.$$

For large deformations (~100% extension), the shear modulus calculated from different membrane laws are related as:

$$G^{\mathrm{NH}} \approx 4G^{\mathrm{SK}}, \quad G^{\mathrm{YE}} \approx 1.99G^{\mathrm{SK}}, \quad \text{and } G^{\mathrm{EV}} \approx 6.4G^{\mathrm{SK}}.$$

We can see that to fit the observed deformation in a certain range, a strain-softening law (like NH or EV) or strain-softening or strain-hardening law (like YE) will predict a higher value of shear modulus than a strain-hardening law (like SK). In the linear regime, all laws will collapse to the same value of G; the value $G \approx 2.5\ \mu$N/m has been reported by Henon *et al.* [47], Waugh and Evans [76], and Wang *et al.* [77] using optical tweezers, micro-pipette aspiration, and LORCA ektacytometer, respectively. Dimitrakopoulos argued that the discrepancy in the value of shear modulus reported using different experimental methods or numerical models is due to the choice of membrane law used to fit data. Additionally, he showed that the Skalak law was the only model to satisfy experimental results from ektacytometry and optical tweezers

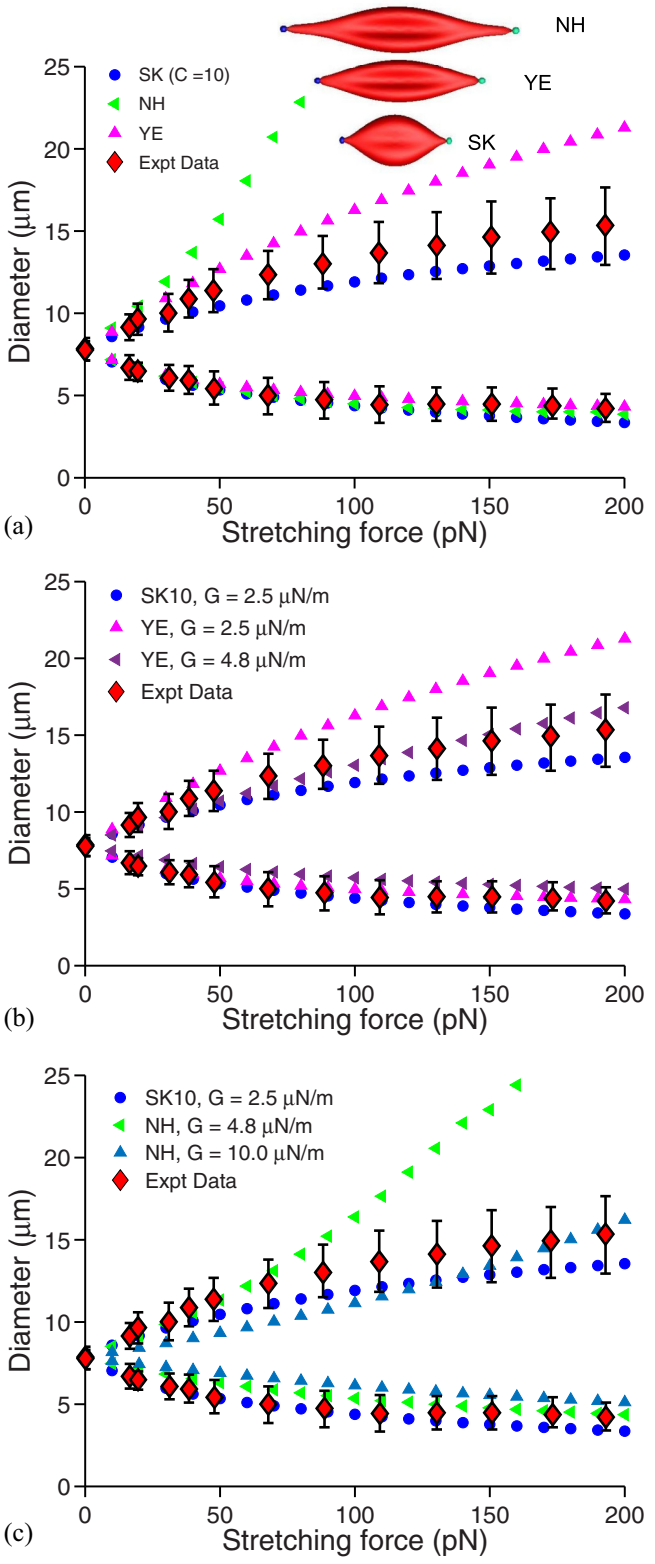

FIG. 5. (Color online) Comparison of numerical predictions for axial and transverse lengths of the RBC against stretching force with experimental optical tweezer results (◊) of Mills *et al.* [48]. (a) Comparison of three different membrane laws at the same shear modulus $G = 2.5\ \mu$N/m; the images show the RBC extension for three different laws at stretching force of 70 pN. (b) Comparison of Yeoh law results at two different shear values of G. (c) Comparison of neo-Hookean law results at two different shear modulus G.

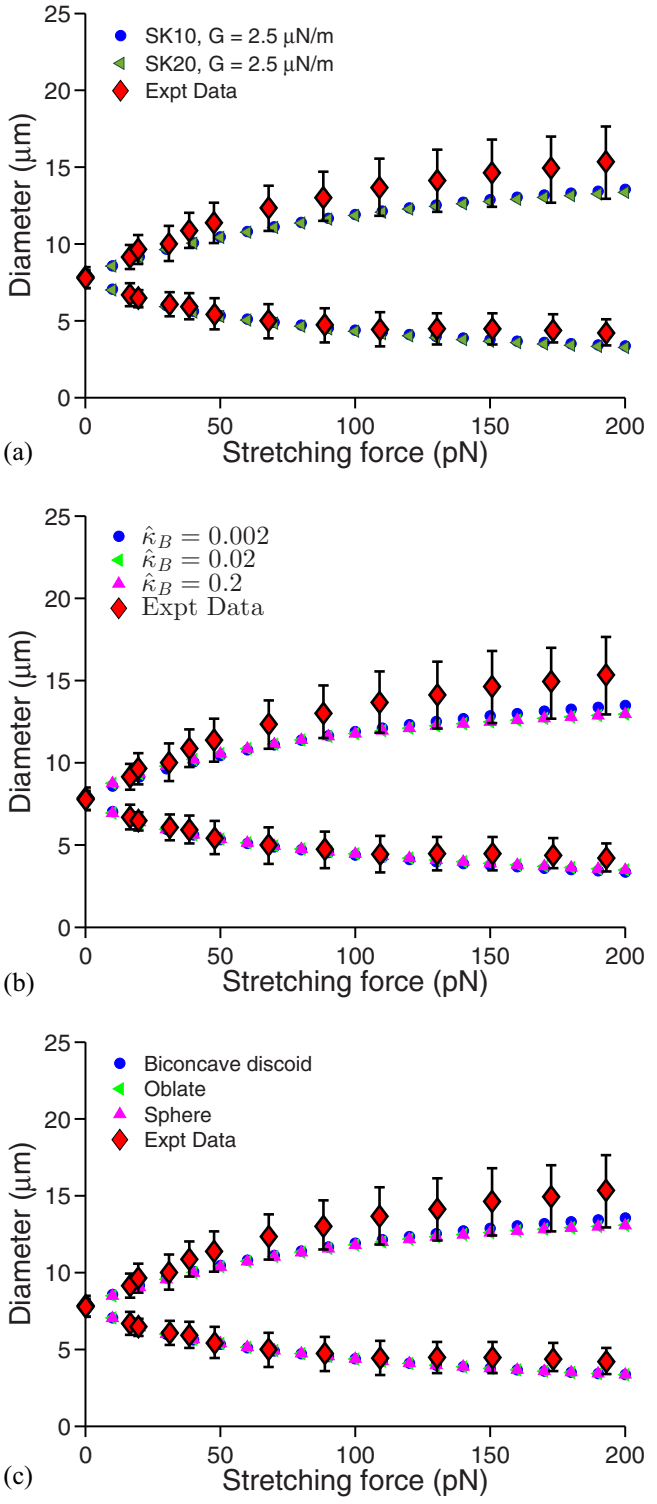

FIG. 6. (Color online) Comparision of numerical variation of axial and transverse lengths of a red blood cell against stretching force with experimental results (◊) of Mills *et al.* [48]. (a) Effect of area dilatational modulus C for the Skalak law at $G = 2.5\ \mu$N/m. (b) Effect of bending modulus $\hat{\kappa}_B$ at $G = 2.5\ \mu$N/m for Skalak (C = 10) law. (c) Effect of spontaneous curvature at $G = 2.5\ \mu$N/m for the Skalak law.

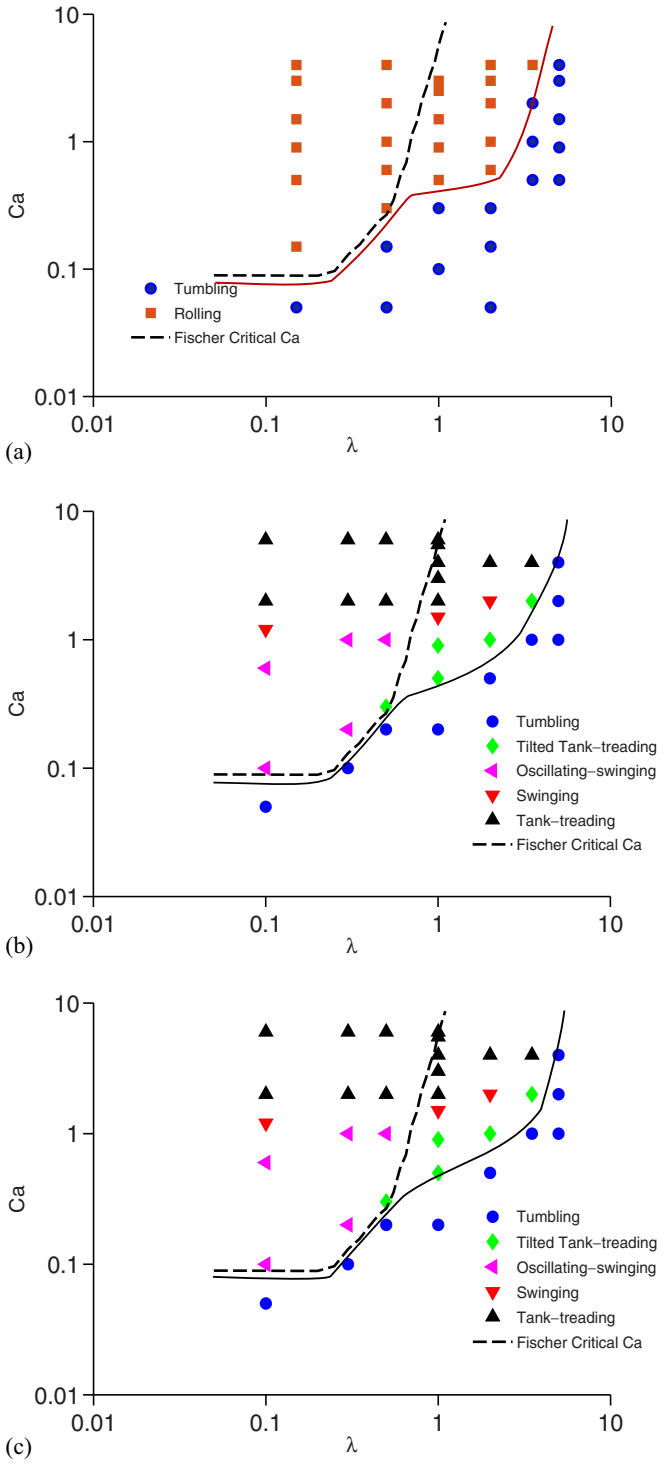

FIG. 7. (Color online) Phase diagram of red-blood-cell dynamics in shear flow for three different spontaneous shapes: (a) biconcave, (b) oblate spheroid, and (c) sphere. The dashed line represents the critical Ca for the TU-TT transition curve from the experimental data of Fischer *et al.* [78], while the solid line separating the two regimes is an approximation based on this work. The values of Ca for experimental data are estimated using $G = 2.5 \times 10^{-6}$ N/m as suggested in Ref. [75] and the viscosity ratio is calculated using an internal viscosity of 5.87 mPa s [44,45].

at moderate and large strains using the value of shear modulus found in the linear regime, i.e., $G = 2.5\ \mu$N/m.

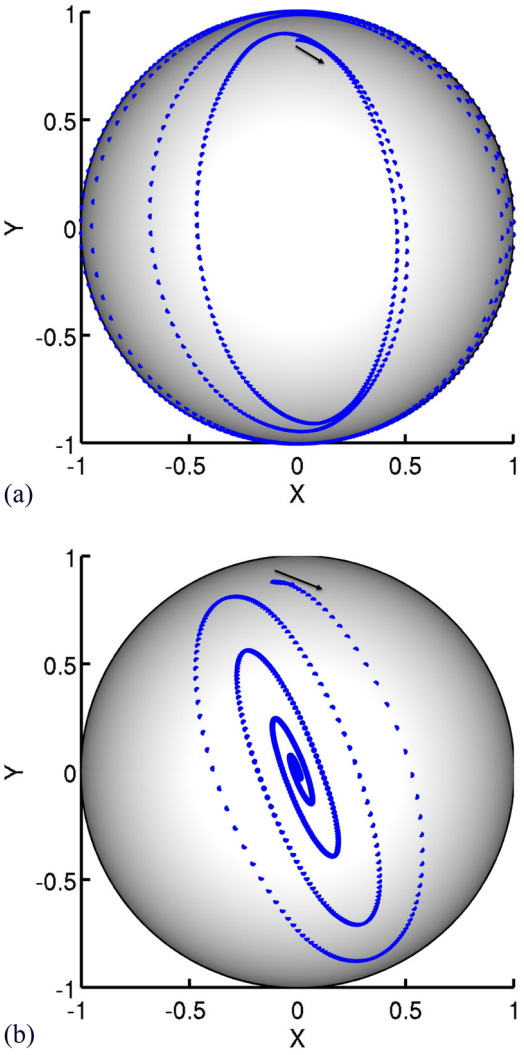

FIG. 8. (Color online) Trajectory on the unit sphere of $\boldsymbol{\psi}_3$ of the RBC. (a) shows a cell approaching TU motion with following simulation conditions: $\lambda = 5$, Ca $= 3.0$, $\xi_0 = \pi/3$, $\hat{\kappa}_B = 0.03$ and biconcave spontaneous curvature. (b) shows a cell approaching rolling motion for the time-lapse image shown in Fig. 9.

In order to validate our RBC model and to test the Dimitrakopoulos analysis, we chose to reproduce the optical tweezer experiment [48] numerically. For this study, the RBC is discretized into 2562 nodes giving 5120 triangular elements. The stretching force is applied to two patches of nodes (2% of the total number of nodes) representing the contact areas of the 2-μm-diameter silica beads used in the experiments. The viscous properties do not affect the final stretching as measurements are done on the final stretched state. Figure 5(a) shows the final axial and transverse cross-sectional lengths of the RBC as a function of applied force for three different membrane laws we studied: Skalak, neo-Hookean, and Yeoh law against the experimental values from Mills *et al.* [48]. The shear modulus for all three membrane laws is taken to be constant value of 2.5 μN/m [47]. We observe that Skalak law fits the experimental data within experimental error for the entire range of applied force while the Yeoh

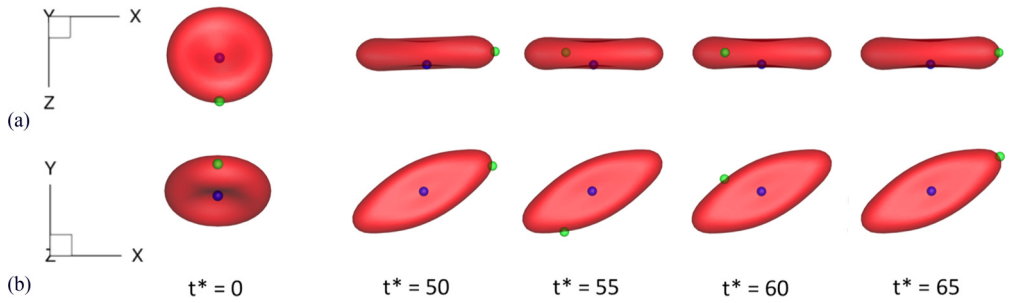

FIG. 9. (Color online) Time sequence images of the RBC in rolling motion in the (a) top view (XZ plane) and (b) side view (XZ plane). Conditions for the simulation were $\lambda = 0.15$, Ca $= 1.5$, $\xi_0 = \pi/6$, $\hat{\kappa}_B = 0.03$ and biconcave spontaneous curvature. Here and in future images, the blue marker dot started at the dimple while the green one started at the rim of the RBC. A brighter marker indicates that it is in front of the cell while a fainter one indicates that it is behind the cell.

and neo-Hookean laws overpredict the RBC stretching due to their strain-softening behavior.

If we apply the Dimitrakopoulos results, the Yeoh law would fit the deformation data for the $G^{\mathrm{YE}} \approx 1.9G^{\mathrm{SK}}$. Keeping in mind that $G^{\mathrm{SK}} = 2.5\ \mu$N/m fits the optical tweezer deformation data, we report the result for $G^{\mathrm{YE}} = 4.8\ \ \mu$N/m $\approx$ 1.9G$^{\mathrm{SK}}$ in Fig. 5(b). For this G^{YE} value the numerical results lie within the error bars of the physical experiment as expected based on the Dimitrakopoulos analysis.

Finally, Fig. 5(c) shows the comparison of the predicted behavior for the neo-Hookean model values of G^{NH} in comparison to the Skalak results with $G^{\mathrm{SK}} = 2.5\ \ \mu$N/m and the experimental data [48]. In the moderate deformation regime, $G^{\mathrm{NH}} = 4.8\ \ \mu$N/m ≈ 2G$^{\mathrm{SK}}$ fits the experimental data

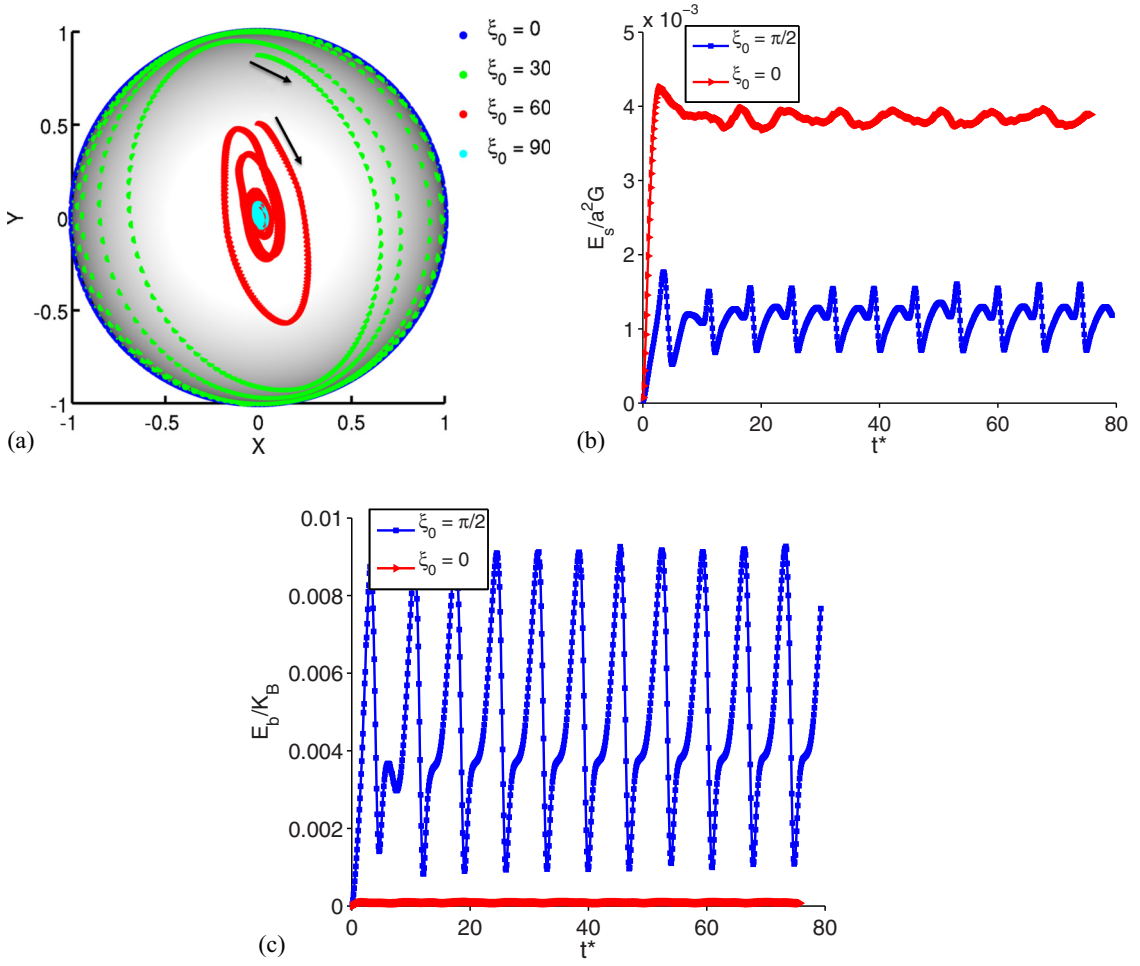

FIG. 10. (Color online) (a) Trajectory of $\boldsymbol{\psi}_3$ on the unit sphere showing the effect of ξ_0 $(0, \pi/6, \pi/3, \pi/2)$ for $\lambda = 3.5$, Ca $= 1.0$, $\hat{\kappa}_B = 0.03$ and biconcave spheroidal spontaneous curvature. The mean membrane (b) elastic and (c) bending energy of the RBC for both rolling (at $\xi_0 = 0$) and TU (at $\xi_0 = \pi/2$) for the case shown in (a).

while at large deformation, $G^{NH} = 10\ \ \mu N/m \approx 4G^{SK}$ fits the experimental data. These observations agree well with the analysis of Dimitrakopoulos [75].

From our comparative analysis of different membrane laws with optical tweezer stretching experiment of Mills *et al.* [48], we confirm not only our RBC model but also the analysis given by Dimitrakopoulos [75] to explain variations in reported values of shear modulus. Based on these results, we employ the Skalak law in our further numerical study.

To assess the dependence of the Skalak law optical tweezer response on the dilatational modulus C, Fig. 6(a) shows results for $G^{SK} = 2.5\ \mu N/m$ and $C = 10$ and $C = 20$ compared against the experimental data [48]. We conclude that the results are insensitive to area incompressibility modulus C for $C \geqslant 10$, in agreement with the conclusions of Barthes-Biesel *et al.* [66].

We also explored the effect of $\hat{\kappa}_B$ as shown in Fig. 6(b). The membrane law used was Skalak with $G^{SK} = 2.5\ \mu N/m$. Value of $\hat{\kappa}_B$ is kept in the range of physiological value predicted in experiments [50]. We notice that varying the bending modulus $\hat{\kappa}_B$ has negligible effect on these stretching results for the RBC membrane.

Deformations in optical tweezer numerical experiments are dominated by shear modulus and membrane laws. Finally, we explored the effect of the spatially varying spontaneous curvature on the optical tweezer results as shown in Fig. 6(c). The Skalak law with $G^{SK} = 2.5\ \mu N/m$ was used for three different spontaneous curvatures: biconcave discoid, oblate spheroid ($V_0 = 0.95$), and sphere. The spontaneous curvature has negligible effect on these stretching results.

IV. RESULTS

A. Effect of spontaneous shape

In this section, we explore the effect of the spontaneous shape of the red blood cell keeping the natural shape for shear elasticity as a biconcave discoid. The simulations were done for viscosity ratio λ in the range of 0.1–5 and Ca was varied between 0.05 and 6. We considered the three cases of spontaneous curvature whose equilibrium shapes are shown in Fig. 2: biconcave discoid, sphere, and oblate spheroid. The constitutive relation for membrane is taken to be the Skalak law with area dilatational modulus $C = 10$ and dimensionless bending modulus $\hat{\kappa}_B = 0.03$. Figure 7 is a summary of the results of the remainder of the paper and we elaborate on these results below: It shows a "phase diagram" of the long-time dynamics of RBCs in shear as a function of Ca and λ for the three different choices of spontaneous curvature. The dashed curve in Fig. 7 represents the experimental data taken from Fischer *et al.* [78] for the critical Ca for TU-TT transition. There are regimes in which the final dynamics depend on the initial off-shear plane orientation. This supports the observation of hysteretic transition regimes seen in experiments of Dupire *et al.* [9] We report the most dominant dynamics (occurring at most ξ_0) in Fig. 7 and a detailed discussion of orientation-dependent dynamics is presented later. We started our simulations at multiple initial orientations $\xi_0 \in [0, \pi/2]$ to study the dynamics of initially out-of-shear plane placed cells. When $\xi_0 = 0$ the axis of revolution is in the vorticity direction, corresponding to the $C = 0$ Jeffery orbit while $\xi_0 = \pi/2$ corresponds to the $C = \infty$ Jeffery orbit where the axis of revolution lies in the shear plane.

Figure 7(a) shows the dynamics of the RBC in λ-Ca parameter space for biconcave spontaneous curvature. We primarily see two dynamical modes here: rolling (see Ref. [79]) at small λ and high Ca and TU at high λ and high Ca. Dynamical modes like swinging and breathing [29] (not shown here) are observed depending on the initial off-shear plane angle ξ_0 and in Fig. 7(a) we have reported the most prevalent dynamical mode at a particular Ca and λ. The attainment of the final stable dynamics is slow and depending on ξ_0 can end up taking several shear time units [33].

We now examine the physiological relevant scenario where $\lambda \approx 5$ while we vary Ca. Here, even at high Ca ($\geqslant 5$), TU is observed. To illustrate the dynamics of an RBC in flow, we calculate the principal axes of the inertia $\boldsymbol{\psi}_1, \boldsymbol{\psi}_2$, and $\boldsymbol{\psi}_3$ of the RBC and report the trajectory of the shortest one, $\boldsymbol{\psi}_3$, on the unit sphere in Fig. 8(a), which shows the approach of an initially off-plane RBC towards TU motion at high Ca. The transition between rolling and TU occurs at progressively lower values of Ca with decreasing viscosity ratio λ. Below a critical viscosity ratio, we find that rolling is the most stable mode even at high Ca. With a biconcave spontaneous shape, we never observe TT and we hypothesize that with this spontaneous curvature, the bending energy required to break away from the biconcave shape is too high even in strong

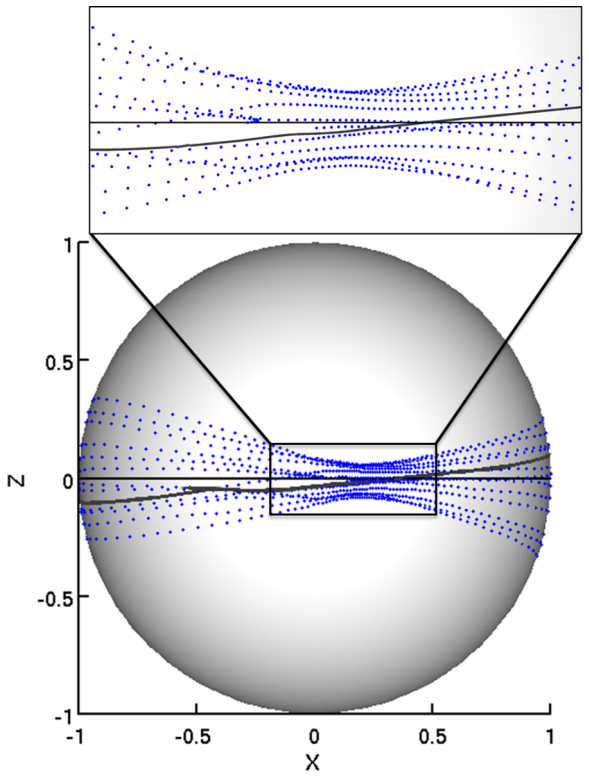

FIG. 11. (Color online) Trajectory of $\boldsymbol{\psi}_3$ on the unit sphere of the RBC exhibiting flip-flopping motion. The gray curve shows the $\boldsymbol{\psi}_3$ trajectory for one flip-flopping event and notice that it crosses shear plane unlike Jeffery orbits. RBC does a combination of off-plane TU and flip-flopping. Conditions for simulation were $\lambda = 1$, Ca = 0.5, $\xi_0 = \pi/2$, $\hat{\kappa}_B = 0.03$ and oblate spheroidal spontaneous curvature.

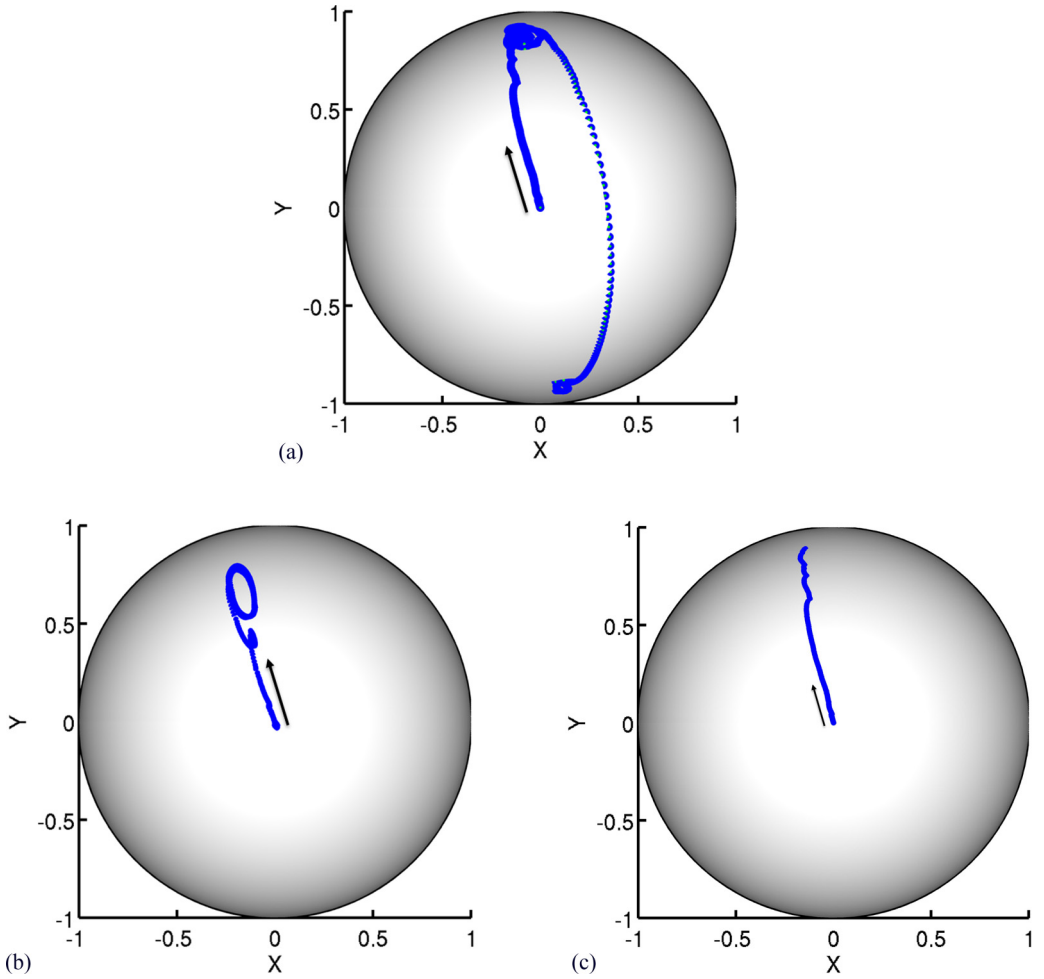

FIG. 12. (Color online) Trajectory of $\boldsymbol{\psi}_3$ projected on a unit sphere for a tilted TT motion. Spontaneous shape is oblate spheroid, $\lambda = 2.0$, $\hat{\kappa}_B = 0.03$ and (a) Ca $= 0.5$, (b) Ca $= 0.6$, and (c) Ca $= 0.75$.

shear flow for TT regime to arise. The trajectory of $\boldsymbol{\psi}_3$ on the unit sphere for a RBC approaching rolling motion is shown in Fig. 8(b). Snapshots of rolling RBC are shown in Fig. 9: These are in good agreement with the experimental results of Dupire *et al.* [9] in which the rolling orbit is stable and the biconcave shape is preserved.

In the transitional regime, we observe that both rolling and TU are stable. Both of them preserve the biconcave shape. One might argue that as shape deviation is minimum in these cases, they minimize the bending energy and hence are stable. However, minimization of energy does not predict the dynamical mode; it is dependent on fluid-structure interactions in a complex way [31,80]. To elaborate on this point, we present the case for $\lambda = 3.5$,Ca $= 1.0$ in Fig. 10, where both rolling (at $\xi_0 = 0$) and TU (at $\xi_0 = \pi/2$) are stable. Both rolling and TU are attractors as a RBC starting at $\xi_0 = \pi/3$ ends up in the TU motion while a RBC starting at $\xi_0 = \pi/6$ ends up in the rolling motion as shown in Fig. 10(a). However, if we look at the mean elastic and bending membrane energy of the RBC in Figs. 10(b) and 10(c), rolling mode has lower membrane bending energy while the TU mode has lower membrane elastic energy.

Last, in Fig. 7(a), the solid curve shows the approximate numerical critical Ca for the transition between rolling and TU while the dashed curve is the experimental Ca for TU-TT transition of the RBC from Fischer *et al.* [78] experiments.

We now turn to Fig. 7(b), which shows the phase diagram for the RBC with oblate spheroidal spontaneous curvature. We would first like to draw attention to a motion that we describe as flip-flopping (see Ref. [79]). Figures 18(e) and 18(f) shows the front and side views, respectively, of a cell going in flip-flopping dynamics. Dupire *et al.* [9] observed the flip-flopping dynamics experimentally, which they called flipping. Flip-flopping differs from TU as, in TU motion, $\boldsymbol{\psi}_3$ of the RBC lies in shear plane all the time while in flip-flopping it does a back-and-forth motion across the shear plane. Note that a normal Jeffery orbit does not cross the shear plane. However, in the side view (XY plane), TU and flip-flopping will be difficult to distinguish as seen in Fig. 18(f). Figure 11 shows the trajectory of $\boldsymbol{\psi}_3$ on a unit sphere for a cell undergoing a combination of TU and flip-flopping. One such flip-flopping trajectory is shown in gray to highlight it.

As Ca is increased, flip-flopping is usually (i.e., at sufficiently high λ) followed by tilted TT (see Ref. [79]), a dynamical motion in which the membrane of the RBC is undergoing TT but $\boldsymbol{\psi}_3$ is not in the shear plane but rather is tilted at an angle to it. Snapshots of tilted TT are shown in Figs. 18(c) and 18(d) in the front and side views, respectively.

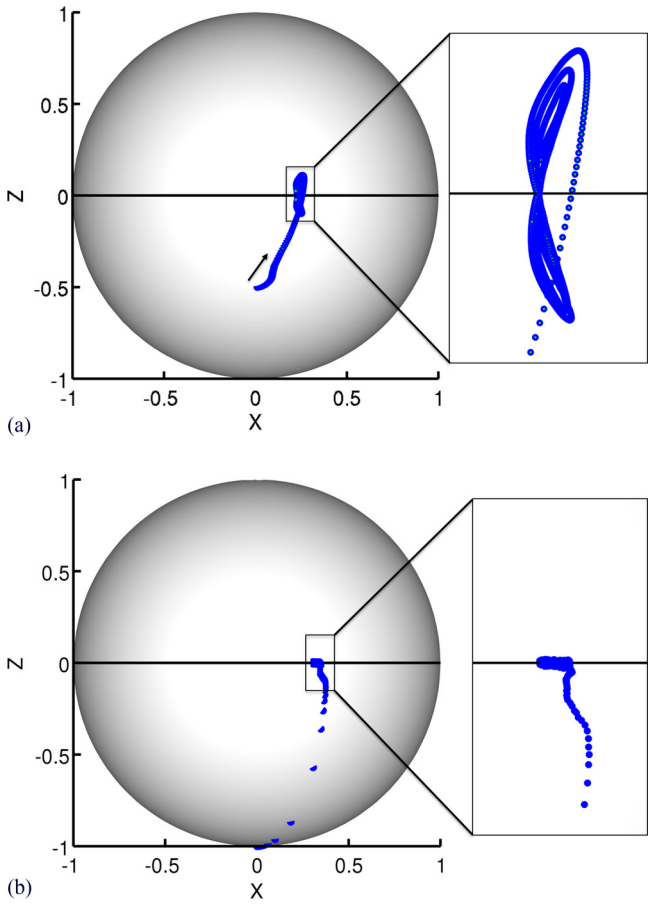

FIG. 13. (Color online) Trajectory of $\boldsymbol{\psi}_3$ on a unit sphere of a RBC exhibiting (a) oscillating-swinging and (b) swinging. Trajectory (a) is for the case in Fig. 14, while (b) is shown for $\lambda = 0.75$, Ca $= 2.0$, $\xi_0 = 0$, $\hat{\kappa}_B = 0.03$ and oblate spheroidal spontaneous curvature. Inset shows a blown-up image of the trajectory near the shear plane.

Dupire *et al.* [9] also observed this motion, which they characterized as a spinning Frisbee motion. They reported it as a transient motion but we find that it is very stable and occurs at small Ca. The detailed dynamics of tilted TT are rather intricate: depending upon the Ca at a particular λ, we see three distinct submotions. Right after the transition from flip-flopping/TU, the cell is tilted at an angle and $\boldsymbol{\psi}_3$ rotates in a small ellipsoidal orbit (which would appear as swinging in the side view) while flipping occasionally as shown in Fig. 12(a). As Ca is increased, flipping of the cell is no longer seen and cell maintains small ellipsoidal orbit, tilted at an angle with shear plane as seen in Fig. 12(b). At even higher Ca, neither flipping nor ellipsoidal orbiting are seen and the RBC stays at a constant angle with the shear plane as shown in Fig. 12(c).

As Ca is further increased, we observe an oscillating-swinging motion in which $\boldsymbol{\psi}_3$ oscillates both in the shear plane and off of it as shown in Fig. 13 and in the images in Fig. 14 executing a "figure 8" trajectory that crosses back and forth across the shear plane. A very similar wobbling motion was first observed numerically by Dupont *et al.* [31] for prolate spheroids and later by Cordasco *et al.* [33] in their red blood cell simulations. Oscillating-swinging is followed by swinging, as Ca is increased at a particular λ. In swinging, $\boldsymbol{\psi}_3$ oscillates only in the shear plane as characterized by Abkarian *et al.* [7]. We point readers to this work for a detailed analysis of swinging.

As Ca is further increased we generally observe the TT motion (see Ref. [79]), where $\boldsymbol{\psi}_3$ points toward wall-normal direction. In Fig. 15, we show images of a cell undergoing TT in both the front and side views and one can observe the dimple while the membrane is moving. Goldsmith and Marlow [1] observed that the RBC retains its dimple even during TT, an observation confirmed in recent experiments by Dupire *et al.* [9] as well. In our simulations, neither biconcave nor spherical spontaneous curvature leads to TT dynamics with a dimple. A very similar conclusion was reached by Peng *et al.* [35] in their study of the effect of nonbiconcave spontaneous curvature on RBC shape. However, Cordasco *et al.* [36], in computations with a spatially uniform spontaneous curvature, noted that they observe TT motion with a dimple for both oblate spheroid and biconcave spontaneous shapes. Nevertheless, given the Peng *et al.* [35] results and our own, we are inclined towards the conclusion that the biconcave spontaneous shape is not the spontaneous shape of the RBC. Additionally, the presence of rich dynamics, including flip-flopping, tilted TT, oscillating-swinging and rolling, all observed in experiments, make oblate spheroid a good candidate for the spontaneous shape of the RBC.

Now having described in detail the dynamics observed with the oblate spheroidal curvature, we revisit Fig. 7(b) to note where we have made some simplifications. We represent TU and flip-flopping with the same symbol as experimentally

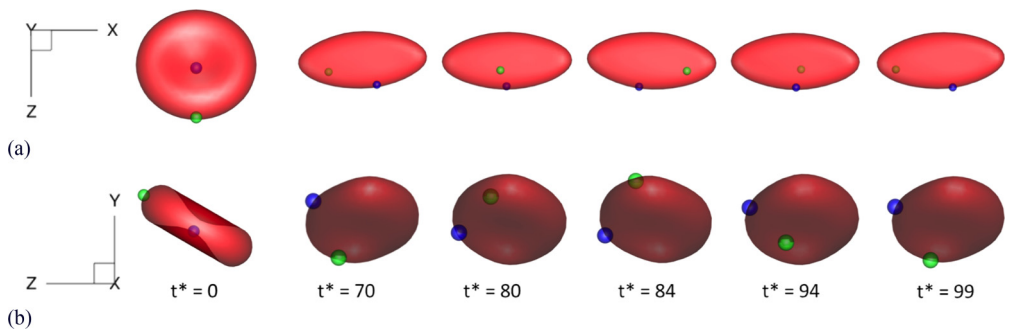

FIG. 14. (Color online) Time sequence images of a RBC performing oscillating-swinging motion in the (a) top view (XZ plane) and (b) front view (YZ plane). Conditions for simulation were: $\lambda = 0.75$, Ca $= 1.0$, $\xi_0 = \pi/3$, $\hat{\kappa}_B = 0.03$ and oblate spheroidal spontaneous curvature. We observe membrane reorientation in oscillating-swinging.

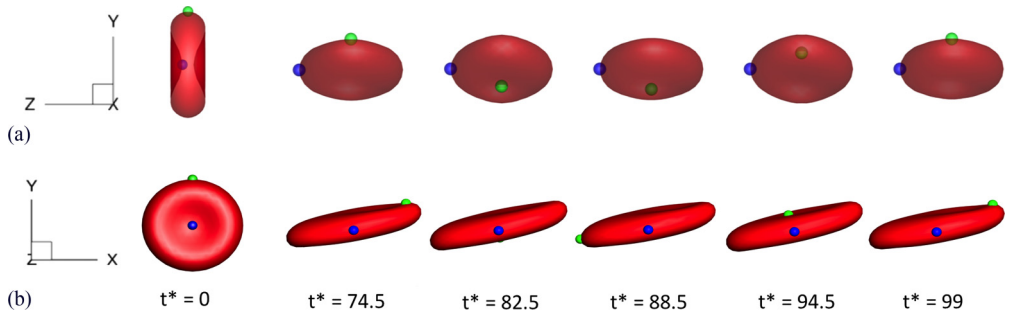

FIG. 15. (Color online) Time sequence images of a RBC performing TT motion in the (a) front view (YZ plane) and (b) side view (YZ plane). Conditions for simulation were: $\lambda = 0.75$, Ca $= 2.0$, $\xi_0 = 0$, $\hat{\kappa}_B = 0.03$ and oblate spheroidal spontaneous curvature. The front view is kept translucent to allow the green material point to be seen, while, in the side view, the YZ plane is tilted by 4° to allow visualization of the dimple.

it will be hard to distinguish between them, especially if looking at them from the side [see Fig. 18(f)]. Furthermore, we have placed oscillating-swinging, swinging, and TT above our numerical TU-TT transition curve in Fig. 7(b) as all three motions are closely related and will resemble TT in experiments. We observe a good agreement with the TU-TT experimental transition curve of Fischer *et al.* [78] for $\lambda \leqslant 0.9$, while at higher λ, the transition in our case happened at a smaller Ca than the one observed in Fischer experiments. Fischer *et al.* [78] suggested that a value of $K_B \sim 20 \times 10^{-19}$ Nm collapses his experimental transition curve and Yazdani *et al.* [29] numerical transition curve onto one curve. We used $K_B \sim 11 \times 10^{-19}$ Nm, which is half of the value suggested by Fischer *et al.* [78] and might be the reason for disagreement at higher λ.

At low λ ($0.12 \leqslant \lambda \leqslant 0.3$), a condition often employed in experiments [1,5–7,9], we see that transition between TU and TT occurs at Ca ≈ 0.15. The associated critical shear stress, $\eta_0\dot{\gamma} \sim \mathrm{Ca}G_s/a_0$ for the TU-TT transition turns out to be $\sim$0.1 Pa, which matches well with the experimental transition shear stress value reported by Bitbol [5] and Dupire *et al.* [9].

Finally, Fig. 7(c) shows the phase diagram of the RBC dynamics for the spherical spontaneous shape. The sphere has been widely studied since the pioneering work of Canham [16] and Helfrich *et al.* [17–19]. The phase diagram for spherical spontaneous shape looks very similar to the phase diagram for oblate spontaneous shape, so we will just point out the primary differences. For the case of spherical spontaneous curvature, in the TU regime, flip-flopping is never observed. However, we do observe kayaking motion, a classical Jeffery orbit with $0 < C < \infty$, which has been recently reported in numerical work for RBCs [36] and vesicles [81,82] dynamics but has not yet been observed experimentally. The kayaking orbits we observed in our numerical simulation were either close to TU or rolling orbits. In Fig. 16, we show the snapshots of kayaking motion in both front and top view and Fig. 17 shows the trajectory of $\boldsymbol{\psi}_3$ of the RBC performing kayaking motion. The motion here is similar to TU. In the other extreme, kayaking looks very similar to rolling or precessing and can be characterized as rolling, unless one looks closely into the trajectory of $\boldsymbol{\psi}_3$. This may be why kayaking has not yet been reported in the experiments.

The other major departure from the oblate spheroidal case is the absence of dimple on the RBC membrane in motions like oscillating-swinging, swinging, and TT. As experiments [1,9] have shown that the cell maintains its biconcave shape, even during TT, the absence of a dimple during TT indicates that a sphere is not likely the spontaneous shape.

In summary, to point out the differences in the final dynamical motion with the choice of spontaneous curvature, we report comparative time-lapse images in Fig. 18 at the same λ and Ca with differing spontaneous curvatures. It is interesting to note that while the biconcave spontaneous shape leads to rolling, the spherical spontaneous shape leads to tilted TT and the oblate spheroidal spontaneous curvature leads to

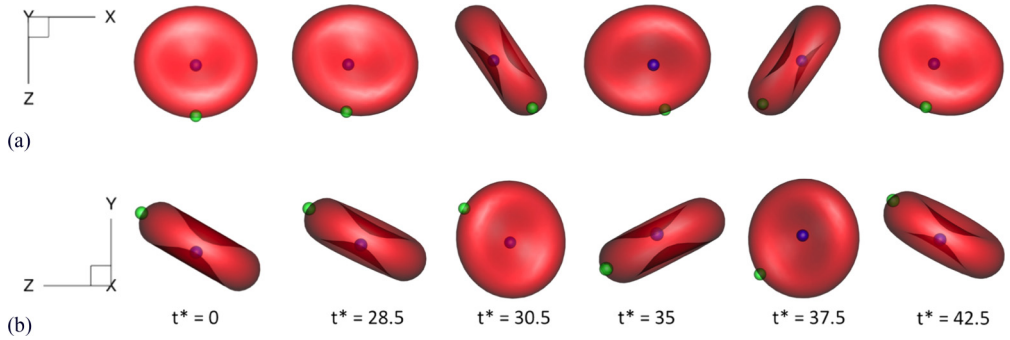

FIG. 16. (Color online) Time sequence images of a RBC in kayaking motion from the (a) top view (XZ plane) and (b) front view (YZ plane), respectively. Conditions for simulation were $\lambda = 5$, Ca $= 1.0$, $\xi_0 = \pi/3$, $\hat{\kappa}_B = 0.03$ and spherical spontaneous curvature. Notice that the membrane reorientation does not happen in kayaking motion.

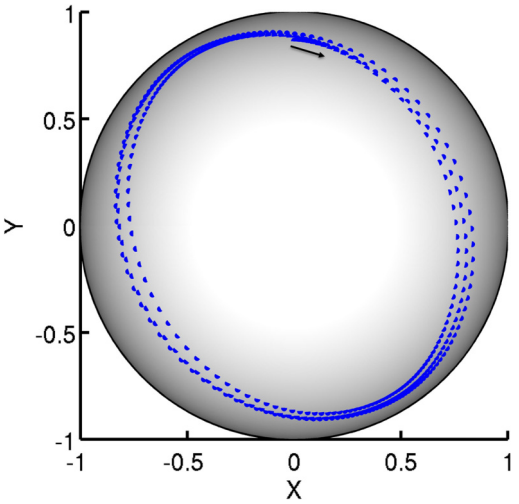

FIG. 17. (Color online) Trajectory of $\boldsymbol{\psi}_3$ on a unit sphere of a RBC performing kayaking motion. Conditions for simulation were identical to those in Fig. 16.

flip-flopping. Figure 18 clearly shows that the choice of the spontaneous shape can strongly affect the final stable dynamics of the RBC. In the light of experimental results of Dupire *et al.* [9], we suggest that the oblate spheroidal shape is the best candidate.

To conclude the section we briefly illustrate the effect of the bending modulus on RBC dynamics. Figure 19 shows the trajectory of $\boldsymbol{\psi}_3$ on the unit sphere of the RBC at three different values of $\hat{\kappa}_B$ at Ca $= 0.5, \lambda = 1, \xi_0 = \pi/2$ with a Skalak law membrane ($C = 10$) and oblate spontaneous shape. At $\hat{\kappa}_B = 0.002$, the RBC performs a swinging motion. With an increase in $\hat{\kappa}_B$ to 0.02, the RBC tumbles, and at $\hat{\kappa}_B = 0.1$ it flip-flops. With increasing $\hat{\kappa}_B$, the penalty for shape change increases, so motions such as swinging that have large bending deformations become increasingly restricted.

B. Membrane reorientation

Finally, we briefly describe an interesting and counterintuitive phenomenon, membrane reorientation, that is observed

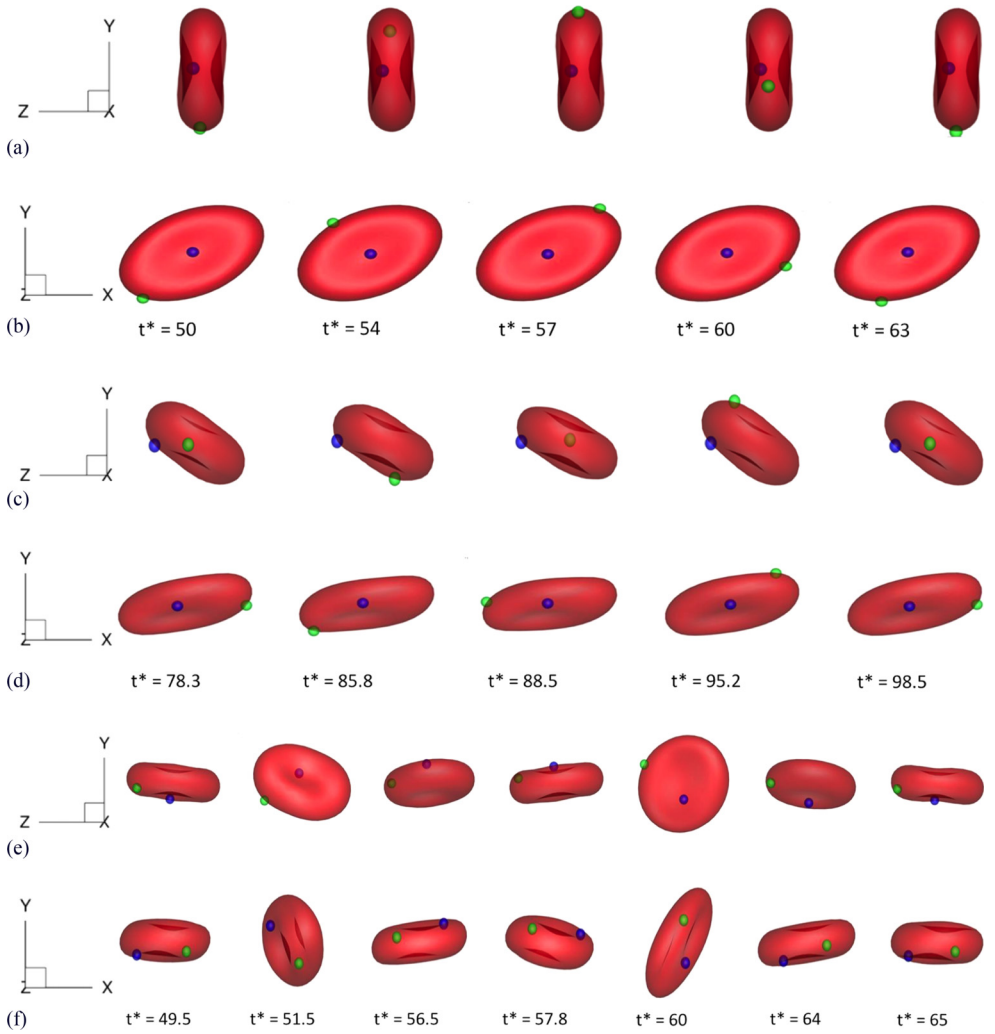

FIG. 18. (Color online) Comparison of cell dynamics at $\lambda = 1$, Ca $= 0.5$, $\hat{\kappa}_B = 0.03$, and $\xi_0 = \pi/3$ for three different spontaneous shapes. [(a) and (b)] Rolling dynamics from front and side view respectively for biconcave spontaneous shape. [(c) and (d)] Tilted tank treading dynamics from the front and side views, respectively, for spherical spontaneous shape. [(e) and (f)] Flip-flopping dynamics from the front and side views, respectively, for oblate spheroidal spontaneous shape.

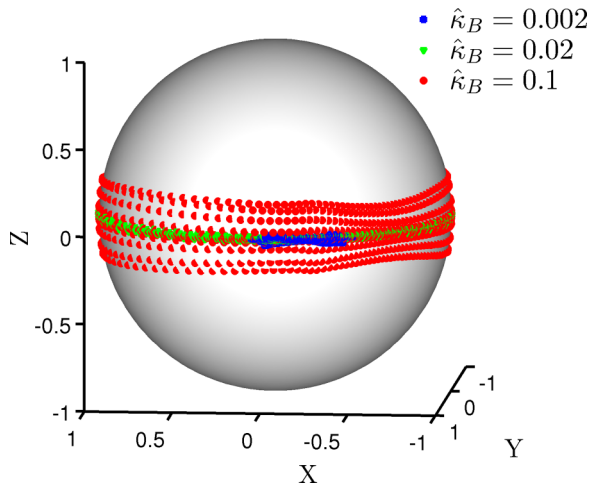

FIG. 19. (Color online) Trajectory of $\boldsymbol{\psi}_3$ on the unit sphere of the RBC showing the effect of $\hat{\kappa}_B$. Conditions for simulation were $\lambda = 1$, Ca $= 0.5$, $\xi_0 = \pi/2$ with SK law ($C = 10$) and oblate spheroidal spontaneous curvature.

in experiments and simulations. Consider a tracer particle attached to the equator of an RBC at rest and another attached to one of the poles. By membrane reorientation, we mean that during flow the one initially at the pole will go to the equator and *vice versa*. Omori *et al.* [83] showed with simulations that this reorientation occurred for both oblate spheroids and RBCs irrespective of the choice of membrane law and Ca. Other studies have also reported the reorientation phenomena [31,33,36]. In the present work, we also observe reorientation in many situations. For the sake of simplicity, we will classify the observed dynamics into two categories: a nonreorientation regime, which includes TU, rolling, kayaking, and flip-flopping, and a reorientation regime, which includes tilted TT, oscillating-swinging, swinging, and TT. Dupire *et al.* [9] characterized what we call the reorientation regime as the "fluidized" regime. In all RBC images shown here the blue and green dots represent a material point on the RBC membrane initially placed at the dimple and the rim, respectively. If we look at the tilted TT dynamics on Figs. 18(c) and 18(d) or at oscillating-swinging on Fig. 14 or TT on Fig. 15, we can clearly see that the blue dot starting from at dimple moves to the rim while the green dot starting at the rim moves to dimple. In contrast, looking at flip-flopping on Figs. 18(e) and 18(f) or at rolling on Fig. 9 or kayaking in Fig. 16, one can observe that the blue dot stays in the dimple region and the green dot stays at the rim.

V. CONCLUSION

We have investigated the dynamics of an RBC subjected to simple shear flow using a membrane bending rigidity model that allows for spatially varying spontaneous curvature, in accordance with experimental observations [15]. The primary aim of this study has been to examine the effect of the varying spontaneous curvature on the dynamical response of the cell in simple shear flow.

To benchmark our RBC model, we computationally reproduced the optical tweezer experiment of Mills *et al.* [48]. Two key findings emerged from this exercise: The first is that the relationship predicted by Dimitrakopoulos [75] between the elastic shear modulus given by different membrane law holds well; the second is that the Skalak strain energy yields good agreement with optical tweezer experimental data using the value of shear modulus that is found in linear regime of stress-strain relation. Additionally, this model is strain hardening and has strong resistance to changes in area as does an RBC membrane. Accordingly, we conclude that is is a good model for use in detailed studies.

Using the Skalak model, we explored the effect of spatially varying nonbiconcave spontaneous curvature on the dynamics of the RBC at capillary scale. Our analysis suggests that oblate spheroid spontaneous shape with the same surface area as the RBC and reduced volume in the range of 0.95–0.989 results in the dynamical motions seen in experiments in the same parameter regime and leads to small deformation from the initial biconcave rest shape. This spontaneous shape leads to better agreement than either a spherical or a biconcave rest shape.

Apart from reporting the effect of spontaneous curvature, we note four other key facts about the RBC dynamics in shear: (i) the net effect of the nonbiconcave spontaneous shape for bending was to make the dimple of the RBC slightly shallower in its rest state than the shape proposed by Evans and Fung [60], as shown in Fig. 2; (ii) there are regions in parameter space where multiple dynamical motions are stable as shown in Fig. 10(a); (iii) during the flip-flopping regime, $\boldsymbol{\psi}_3$ of the RBC crosses the shear plane as shown in Fig. 11, a behavior that differs considerably from a Jeffery orbit; and (iv) the different dynamics can be categorized broadly into two regimes, (a) a nonreorientation regime where membrane elements originally at the rim of the cell remain there and (b) a reorientation regime, where the part of membrane forming the dimple goes to the rim and vice versa.

ACKNOWLEDGMENTS

This work was supported by NSF Grants No. CBET-0852976 (funded under the American Recovery and Reinvestment Act of 2009), No. CBET-1132579, and No. CBET-1436082 as well as a graduate fellowship from BP to Kushal Sinha.

APPENDIX

We will apply the tools of differential geometry in order to derive Eq. (4) from Eq. (1). The membrane Γ of the RBC can be represented as a closed surface in Euclidean three-dimensional space; position on the membrane is given by the vector $\boldsymbol{R}(u,v)$, where (u,v) are curvilinear coordinates on the surface. We recall the principal definitions of differential geometry to introduce the following quantities and refer to Refs. [61,62,84] for details:

$$\begin{aligned} &\boldsymbol{R}_i = \partial_i \boldsymbol{R}, && \boldsymbol{R}_{ij} = \partial_i \partial_j \boldsymbol{R}, && g_{ij} = \boldsymbol{R}_i \cdot \boldsymbol{R}_j, \\ &g^{ij} = (g_{ij})^{-1}, && g = \det(g_{ij}), && L_{ij} = \boldsymbol{R}_{ij} \cdot \boldsymbol{n}, \\ &L^{ij} = (L_{ij})^{-1}, && L = \det(L_{ij}) && (i,j = 1,2), \end{aligned} \tag{A1}$$

where $\partial_1 = \partial_u$, $\partial_2 = \partial_v$, $\boldsymbol{R}_i$ is the tangent vector to the surface and g_{ij} and L_{ij} are the induced metric and extrinsic curvature associated with the first and second fundamental forms of the

surface, respectively. Repeated indices imply summation. The normal vector $\boldsymbol{n}$ and the Christoffel symbols Γ^k_{ij} are defined as

$$\boldsymbol{n} = (\boldsymbol{R}_1 \times \boldsymbol{R}_2)/\sqrt{g}, \boldsymbol{R}_{ij} = \Gamma^k_{ij}\boldsymbol{R}_k + L_{ij}\boldsymbol{n}. \quad \text{(A2)}$$

The mean and Gaussian curvature are written, respectively, as

$$\kappa_H = -\frac{1}{2}(c_1 + c_2) = \frac{1}{2}g^{ij}L_{ij}, \kappa_G = c_1 c_2 = L/g. \quad \text{(A3)}$$

Here c_1 and c_2 are the two principal curvatures. The Canham-Helfrich Hamiltonian $\mathcal{H}$ [first term in Eq. (1)] is given as

$$\mathcal{H} = \frac{K_B}{2}\int_\Gamma (2\kappa_H + c_0)^2 dS = \int_\Gamma h dS, \quad \text{(A4)}$$

where the scalar $h = \frac{K_B}{2}(2\kappa_H + c_0)^2$ is constructed locally from the geometry of surface and $dS = \sqrt{g}\, du\, dv$. The stress (force density) $\boldsymbol{f}$ associated with $\mathcal{H}$ is determined from the knowledge of the response of the Hamiltonian $\delta\mathcal{H}$ to an arbitrary infinitesimal deformation $\delta\boldsymbol{R}$ using the principle of virtual work:

$$\delta\mathcal{H} = \int_\Gamma \boldsymbol{f}\cdot\delta\boldsymbol{R} dS. \quad \text{(A5)}$$

We can decompose $\delta\boldsymbol{R}$ into its tangential and normal parts [62],

$$\delta\boldsymbol{R} = \zeta^i \boldsymbol{R}_i + \Phi\boldsymbol{n}. \quad \text{(A6)}$$

Likewise, infinitesimal change in the Hamiltonian can be decomposed into its tangential and normal parts [62],

$$\delta\mathcal{H} = \delta_\parallel\mathcal{H} + \delta_\perp\mathcal{H}. \quad \text{(A7)}$$

We will first look into the tangential part. For any scalar function $f(u,v)$ defined on Γ, $\delta_\parallel f = \zeta^i\partial_i f$, and under tangential deformation, the induced metric on Γ transforms as a Lie derivative, $\delta_\parallel\sqrt{g} = \partial_i(\sqrt{g}\zeta^i)$. Using the above definitions, the tangential component of Hamiltonian is

$$\begin{aligned}\delta_\parallel\mathcal{H} &= \int_\Gamma \{\sqrt{g}(\delta_\parallel h) + (\delta_\parallel\sqrt{g})h\}\, du\, dv \\ &= \int_\Gamma \{\sqrt{g}(\zeta^i\partial_i h) + h\partial_i(\sqrt{g}\zeta^i)\}\, du\, dv \\ &= \int_\Gamma \zeta^i\partial_i h\sqrt{g}\, du\, dv = \int_\Gamma \zeta^i\partial_i h\, dS. \end{aligned} \quad \text{(A8)}$$

The integrand in the last equation is simply the surface gradient of scalar h. Thus, the tangential component of the stress can be given as

$$\boldsymbol{f}_\parallel = \nabla_s h = \frac{K_B}{2}\nabla_s\{(2\kappa_H + c_0)^2\}. \quad \text{(A9)}$$

For the normal term, we note from Ref. [61]

$$\begin{aligned}\delta_\perp\int_\Gamma dS &= -\int_\Gamma 2\Phi\kappa_H dS \\ \delta_\perp\kappa_H &= \Phi(2\kappa_H{}^2 - \kappa_G) + \frac{1}{2}g^{ij}\left(\Phi_{ij} - \Gamma^k_{ij}\Phi_k\right),\end{aligned} \quad \text{(A10)}$$

where $\Phi_i = \partial_i\Phi$. The normal variation in Hamiltonian is given as

$$\begin{aligned}\delta_\perp\mathcal{H} &= \frac{K_B}{2}\delta_\perp\int_\Gamma (2\kappa_H + c_0)^2 dS \\ &= \frac{K_B}{2}\int_\Gamma [(2\kappa_H + c_0)^2\delta_\perp dS + 4(2\kappa_H + c_0)\delta_\perp\kappa_H] dS \\ &= K_B\int_\Gamma \Phi\big[(2\kappa_H + c_0)\big(2\kappa_H^2 - 2\kappa_G - c_0\kappa_H\big) + \big\{(1/\sqrt{g})\big(\partial_i\partial_j + \partial_k\Gamma^k_{ij}\big)g^{ij}\sqrt{g}\big\}(2\kappa_H + c_0)\big] dS \\ &= K_B\int_\Gamma \Phi\big[(2\kappa_H + c_0)\big(2\kappa_H^2 - 2\kappa_G - c_0\kappa_H\big) + (1/\sqrt{g})\partial_i(g^{ij}\sqrt{g}\partial_j)(2\kappa_H + c_0)\big] dS \\ &= K_B\int_\Gamma \Phi\big[(2\kappa_H + c_0)\big(2\kappa_H^2 - 2\kappa_G - c_0\kappa_H\big) + \Delta_s(2\kappa_H + c_0)\big] dS,\end{aligned} \quad \text{(A11)}$$

where we have used Eq. (A10) and the following identities [61]:

$$\begin{aligned}\partial_i[(\partial_j g^{ij}\sqrt{g})f] &= -\partial_k(\Gamma^k_{ij}g^{ij}\sqrt{g}f) \\ \Delta_s &= (1/\sqrt{g})\partial_i(g^{ij}\sqrt{g}\partial_j).\end{aligned} \quad \text{(A12)}$$

Thus the normal component of the force is

$$\begin{aligned}\boldsymbol{f}_\perp = K_B\big[&(2\kappa_H + c_0)\big(2\kappa_H^2 - 2\kappa_G - c_0\kappa_H\big) \\ &+ \Delta_s(2\kappa_H + c_0)\big]\boldsymbol{n}.\end{aligned} \quad \text{(A13)}$$

[1] H. Goldsmith and J. Marlow, Proc. R. Soc. B **182**, 351 (1972).
[2] H. Schmid-Schönbein and R. Wells, Science **165**, 288 (1969).
[3] T. M. Fischer, M. Stöhr-Liesen, and H. Schmid-Schönbein, Science **202**, 894 (1978).
[4] R. Skalak and P. Branemark, Science **164**, 717 (1969).
[5] M. Bitbol, Biophys. J. **49**, 1055 (1986).
[6] W. Yao, Z. Wen, Z. Yan, D. Sun, W. Ka, L. Xie, and S. Chien, J. Biomech. **34**, 1501 (2001).

[7] M. Abkarian, M. Faivre, and A. Viallat, Phys. Rev. Lett. **98**, 188302 (2007).
[8] J. Dupire, M. Abkarian, and A. Viallat, Phys. Rev. Lett. **104**, 168101 (2010).
[9] J. Dupire, M. Socol, and A. Viallat, Proc. Natl. Acad. Sci. USA **109**, 20808 (2012).
[10] G. B. Jeffery, Proc. R. Soc. A **102**, 161 (1922).
[11] S. R. Keller and R. Skalak, J. Fluid Mech. **120**, 27 (1982).
[12] J. M. Skotheim and T. W. Secomb, Phys. Rev. Lett. **98**, 078301 (2007).
[13] E. Evans and R. Hochmuth, Biophys. J. **16**, 1 (1976).
[14] T. Secomb and R. Skalak, Microvasc. Res. **24**, 194 (1982).
[15] T. M. Fischer, Biophys. J. **86**, 3304 (2004).
[16] P. Canham, J. Theor. Biol. **26**, 61 (1970).
[17] W. Helfrich, Z. Naturforsch., Teil C **28**, 693 (1973).
[18] W. Helfrich and H. J. Deuling, J. Phys. Colloques **36**, C1-327 (1975).
[19] H. Deuling and W. Helfrich, Biophys. J. **16**, 861 (1976).
[20] P. Zarda, S. Chien, and R. Skalak, J. Biomech. **10**, 211 (1977).
[21] T. Fischer, C. Haest, M. Stöhr-Liesen, H. Schmid-Schönbein, and R. Skalak, Biophys. J. **34**, 409 (1981).
[22] G. Lim H. W., M. Wortis, and R. Mukhopadhyay, Proc. Natl. Acad. Sci. USA **99**, 16766 (2002).
[23] S. Ramanujan and C. Pozrikidis, J. Fluid Mech. **361**, 117 (1998).
[24] C. Pozrikidis, Ann. Biomed. Eng. **31**, 1194 (2003).
[25] Y. Sui, H. T. Low, Y. T. Chew, and P. Roy, Phys. Rev. E **77**, 016310 (2008).
[26] H. Zhao, A. Isfahani, L. Olson, and J. Freund, J. Comput. Phys. **229**, 3726 (2010).
[27] D. A. Fedosov, B. Caswell, and G. E. Karniadakis, Biophys. J. **98**, 2215 (2010).
[28] W. R. Dodson III and P. Dimitrakopoulos, Phys. Rev. E **84**, 011913 (2011).
[29] A. Z. K. Yazdani and P. Bagchi, Phys. Rev. E **84**, 026314 (2011).
[30] A. Farutin, T. Biben, and C. Misbah, J. Comput. Phys. **275**, 539 (2014).
[31] C. Dupont, A.-V. Salsac, and D. Barthès-Biesel, J. Fluid Mech. **721**, 180 (2013).
[32] Z. Wang, Y. Sui, P. D. M. Spelt, and W. Wang, Phys. Rev. E **88**, 053021 (2013).
[33] D. Cordasco and P. Bagchi, Phys. Fluids **25**, 091902 (2013).
[34] C. Pozrikidis, Math. Med. Biol. **22**, 34 (2005).
[35] Z. Peng, A. Mashayekh, and Q. Zhu, J. Fluid Mech. **742**, 96 (2014).
[36] D. Cordasco, A. Yazdani, and P. Bagchi, Phys. Fluids **26**, 041902 (2014).
[37] J. E. Rothman and J. Lenard, Science **195**, 743 (1977).
[38] S. M. Gruner, Proc. Natl. Acad. Sci. USA **82**, 3665 (1985).
[39] H. T. McMahon and J. L. Gallop, Nature **438**, 590 (2005).
[40] J. Zimmerberg and M. M. Kozlov, Nat. Rev. Mol. Cell Biol. **7**, 9 (2006).
[41] F. Campelo and V. Malhotra, Annu. Rev. Biochem. **81**, 407 (2012).
[42] B. Antonny, Annu. Rev. Biochem. **80**, 101 (2011).
[43] G. Lowe and J. Barbenel, in *Clinical Blood Rheology*, Vol. 1 (CRC Press, Boca Raton, FL, 1988).
[44] G. R. Cokelet and H. J. Meiselman, Science **162**, 275 (1968).
[45] N. Mohandas and P. G. Gallagher, Blood **112**, 3939 (2008).
[46] W. Linss, C. Pilgrim, and H. Feuerstein, Acta Histochem. **91**, 101 (1991).
[47] S. Henon, G. Lenormand, A. Richert, and F. Gallet, Biophys. J. **76**, 1145 (1999).
[48] J. Mills, L. Qie, M. Dao, C. Lim, S. Suresh *et al.*, Molecular and Cellular Biomechanics **1**, 169 (2004).
[49] T. Betz, M. Lenz, J.-F. Joanny, and C. Sykes, Proc. Natl. Acad. Sci. USA **106**, 15320 (2009).
[50] J. Evans, W. Gratzer, N. Mohandas, K. Parker, and J. Sleep, Biophys. J. **94**, 4134 (2008).
[51] R. Lipowsky, Nature **349**, 475 (1991).
[52] A. Libai and J. G. Simmonds, *The Nonlinear Theory of Elastic Shells* (Cambridge University Press, Cambridge, 2005).
[53] U. Seifert, K. Berndl, and R. Lipowsky, Phys. Rev. A **44**, 1182 (1991).
[54] D. Steigmann and R. Ogden, Proc. R. Soc. A **455**, 437 (1999).
[55] D. V. Le, Phys. Rev. E **82**, 016318 (2010).
[56] W.-X. Huang, C. B. Chang, and H. J. Sung, J. Comput. Phys. **231**, 3340 (2012).
[57] C. Pozrikidis, J. Comput. Phys. **169**, 250 (2001).
[58] D. Discher, N. Mohandas, and E. Evans, Science **266**, 1032 (1994).
[59] D. E. Discher, D. H. Boal, and S. K. Boey, Biophys. J. **75**, 1584 (1998).
[60] E. Evans and Y. Fung, Microvasc. Res. **4**, 335 (1972).
[61] Ou-Yang Zhong-can and W. Helfrich, Phys. Rev. A **39**, 5280 (1989).
[62] R. Capovilla and J. Guven, J. Phys. A: Math. Gen. **35**, 6233 (2002).
[63] C. Canuto, M. Y. Hussaini, A. Quarteroni, and T. A. Zang, *Spectral Methods in Fluid Dynamics* (Springer, New York, 1988).
[64] R. Skalak, A. Tozeren, R. P. Zarda, and S. Chien, Biophys. J. **13**, 245 (1973).
[65] D.-V. Le, J. White, J. Peraire, K. Lim, and B. Khoo, J. Comput. Phys. **228**, 8427 (2009).
[66] D. Barthes-Biesel, A. Diaz, and E. Dhenin, J. Fluid Mech. **460**, 211 (2002).
[67] O. Yeoh, Rubber Chem. Technol. **63**, 792 (1990).
[68] M. Meyer, M. Desbrun, P. Schröder, and A. H. Barr, in *Visualization and Mathematics III* (Springer, Berlin, 2003), pp. 35–57.
[69] G. Boedec, M. Leonetti, and M. Jaeger, J. Comput. Phys. **230**, 1020 (2011).
[70] J. M. Charrier, S. Shrivastava, and R. Wu, J. Strain Anal. Eng. Des. **22**, 115 (1987).
[71] C. Pozrikidis, *Boundary Integral and Singularity Methods for Linearized Viscous Flow* (Cambridge University Press, Cambridge, 1992).
[72] A. Kumar and M. D. Graham, J. Comput. Phys. **231**, 6682 (2012).
[73] J. P. Hernández-Ortiz, J. J. de Pablo, and M. D. Graham, Phys. Rev. Lett. **98**, 140602 (2007).
[74] D.-V. Le and S. T. Wong, J. Comput. Phys. **230**, 3538 (2011).
[75] P. Dimitrakopoulos, Phys. Rev. E **85**, 041917 (2012).
[76] R. Waugh and E. Evans, Biophys. J. **26**, 115 (1979).
[77] X. Wang, H. Zhao, F. Zhuang, and J. Stoltz, Clin. Hemorheol. Microcirc. **21**, 291 (1999).
[78] T. M. Fischer and R. Korzeniewski, J. Fluid Mech. **736**, 351 (2013).

[79] See Supplemental Material at http://link.aps.org/supplemental/10.1103/PhysRevE.92.042710 for movies of RBC dynamics.
[80] T. Omori, T. Ishikawa, Y. Imai, and T. Yamaguchi, J. Fluid Mech. **724**, 154 (2013).
[81] T. Biben, A. Farutin, and C. Misbah, Phys. Rev. E **83**, 031921 (2011).
[82] A. P. Spann, H. Zhao, and E. S. Shaqfeh, Phys. Fluids **26**, 031902 (2014).
[83] T. Omori, Y. Imai, T. Yamaguchi, and T. Ishikawa, Phys. Rev. Lett. **108**, 138102 (2012).
[84] E. Kreyszig, *Differential Geometry* (Dover, London, 1991).